LA-UR- 97-2901

Title: R&D – SEISMIC REPORT ON THE INFLUENCE OF
THE SOURCE REGION ON REGIONAL SEISMIC
WAVEFORMS AS INFERRED FROM MODELING.

Author(s): FRED N. APP
ERIC N. JONES
RANDALL J. BOS

RECEIVED
NOV 1 2 1997
OSTI

Submitted to: DEPARTMENT OF ENERGY, COMPREHENSIVE TEST
BAN TREATY R & D, NN-20

MASTER

DISCLAIMER

DISTRIBUTION OF THIS DOCUMENT IS UNLIMITED

Los Alamos
NATIONAL LABORATORY

Form 836 (10/96)

DISCLAIMER

Portions of this document may be illegible in electronic image products. Images are produced from the best available original document.

R&D-Seismic Report on the Influence of the Source Region on Regional Seismic Waveforms as Inferred from Modeling.

Fred N. App
Eric M. Jones
Randall J. Bos

Abstract

The identification of an underground nuclear test from its seismic signal recorded by seismometers at regional distances is one of the fundamental scientific goals of the Comprehensive Test Ban Treaty R&D Program. The work being reported here addresses the issue of event discrimination through the use of computer models that use realistic simulations of nuclear explosions in various settings for the generation of near-regional and regional synthetic seismograms. The study exercises some unique, recently developed computer modeling capabilities that heretofore have not been available for discrimination studies. A variety of source conditions and regional paths are investigated. Under the assumptions of the study, our conclusions are: 1) spall, non-linear deformation, and depth-of-burial do not substantially influence the near-regional signal and 2) effects due to basins along the regional path very much dominate over source region geology in influencing the signal at regional distances. These conclusions, however, are relevant only for the frequencies addressed, which span the range from 0.1 to 1 Hz for the regional calculations and 0.1 to 3 Hz for the near-regional calculations. They also are relevant only for the crudely "China-like" basin, crust, and mantle properties used in the study. If it is determined that further investigations are required, researchers may use this study as a template for such work.

Introduction

This report contains results of calculations that use realistic simulations of nuclear explosions in various settings in the generation of near-regional and regional synthetic seismograms. The objectives are to determine the relative importance of source configuration, inelasticity, spall and close-in geology in seismic wave generation and the potential for detection of such close-in effects at regional distances when various regional path effects are introduced. The study deals only with underground nuclear explosions and it exercises some unique, recently developed, modeling capabilities that heretofore have not been available for looking at the issues involved for this class of seismic source. We selected cases that, for the most part, represent extremes in source conditions, but by no means do we claim that all the relevant and potentially crucial cases are covered. The approach followed in this study can be used as a template for continuing this research.

Background

Close-in nuclear explosion phenomenology has been studied extensively as part of the United States Underground Nuclear Test Program. Codes and methodologies have been developed for systematically studying how the earth responds to an underground explosion. A wealth of measurements exist for validation of these computer models. The community dealing with the containment of underground nuclear explosions has been most active in this area. There are two reports authored by Los Alamos researchers (App and Brunish, 1991; App and Brunish, 1992) that describe in considerable detail the ground motion associated with contained underground

nuclear explosions. Other useful references related to ground motion modeling in general are Glenn (1993) and Rimer et al. (1989).

There are five elements of a signal from a normally-buried nuclear explosion that are of interest for seismic wave propagation: 1) an elastic precursor, 2) the elastic remnant of the non-linear "plastic" wave, 3) spall, 4) spall recompaction and 5) elastic rebound. The elastic precursor runs ahead of the main signal and its amplitude is determined by the threshold strength of the rock. The form of the elastic remnant of the plastic wave is a very strong function of the non-linear response of the rock during the close-in crushing and shear failure phases. During non-linear deformation, the wave shape undergoes severe changes; its final form for seismic propagation is that attained at the time the wave amplitude decays to the point of becoming elastic, thus the name "elastic remnant". Inelasticity can have a significant influence on the frequency content of the initial elastic signal for seismic wave propagation. Spall and spall closure are surface effects and the manner in which they can influence the seismic signal is one objective of this study. The mechanism of spall and how it is manifested in a variety of settings is the subject of the App and Brunish (1992) report. From the standpoint of a seismic signal source, elastic rebound is of interest primarily because it is vertically asymmetrical. Elastic rebound is associated with the first expansion and rebound of the explosion-produced cavity. The combination of a nearby free surface, increasing overburden pressure with depth, and the usual rapid increase in sound speed and rock strength with depth can cause the elastic rebound to be highly asymmetrical, with rebound typically occurring first beneath the explosion point, then from the sides, and finally from the top. From bottom to top, the rebound signals can be as much as 180 degrees out of phase with one other.

A further point to be made regarding a tamped nuclear explosion is that only a small fraction of the total energy is transmitted into the elastic regime as seismic waves. Typical values range from a few percent in hard rock to a few tenths of a percent in unconsolidated soils and alluvium (App, 1993). All potentially important elements of an underground nuclear explosion are not captured in elastic moment tensor descriptions; however, in this study all elements are included in the source description through the use of strong-motion "weapons effects" computer codes.

The five elements discussed above are characteristics of a tamped, underground nuclear explosion, however, they may also be observed in association with a large, "point source" conventional explosion such as occurred with the non-proliferation experiment (NPE) at the Nevada Test Site (NTS) (Kamm and Bos, 1995, Stump et al., 1994).

General Approach

Cases of coupling the results of non-linear simulations to wave-propagation codes have been described in Bache et al. (1982) and McLaughlin et al.(1988). More recently, Taylor and App (1994) followed basically the same techniques in coupling Los Alamos non-linear weapons-effects codes to a reflectivity code. This newly developed coupling capability was applied in the analysis of the NTS DIVIDER and CORREO events (App et al., 1995) with some promising results. The essence of what was determined was that a considerably lower Pg/Lg ratio was both observed and calculated for the structurally uncomplicated CORREO event than for the DIVIDER event that was located next to a large fault scarp. The calculations showed that the fault scarp actually suppressed conversion of P to S along the Tertiary/Paleozoic (soft rock/hard rock) boundary present at the site, resulting in a weaker Lg for DIVIDER. A deficiency of the calculations, however, was that the regional structure could be modeled only as flat, horizontal layers. In this particular instance, the flat-layer simplification provided a result that agreed with experimental data, but we should not count on this always being the case. Using the reflectivity code in its current form, it is impossible to address the influence of structure along the regional path on the regional signal.

In order to compensate for this deficiency, the Los Alamos Geodynamics Team developed a two–dimensional/three–dimensional elastic-anelastic finite-difference code named AFD (Kamm, et al., 1996) and, as well, the associated software for allowing linkage between it and the strong-motion, weapons-effects codes. The linkage approach is shown in Figure 1. In theory, this provides us with a capability for addressing problems of any complexity both close-in and at regional

distances. In practice, however, there are some very limiting factors, the main one being computer size and power. Even the most advanced high-performance computers envisioned for the end of this century will not allow us to calculate synthetics with the level of detail we prefer. Our ultimate goal is to calculate synthetic seismograms to regional distances in 3-D structure with up to 10 Hz frequency resolution. Enhancements need to be made to both computing software and hardware before this objective can be met.

This brings us to the current work. As mentioned earlier, this study can be considered a template for future work as capabilities improve. Because of current restrictions in the application of the AFD code, all calculations reported here are at either 1 or 3 Hz frequency resolution and are limited to two dimensions. The calculations are, however, carried out to regional distances of up to 1700 km. The only weapons-effects code employed in this study is a Los Alamos modified version of the Sandia Laboratory code TOODY (Swegle, 1978); however, such coupling also can be performed using the Los Alamos codes SMC (Dey and Kamm, 1995) and RAGE (Los Alamos National Laboratory, 1997) as well. The Los Alamos version of TOODY includes gravity, overburden stress, and various material constitutive laws for simulating the inelastic deformation and damage of rock. The code is used to model such effects as shock heating, vaporization, melt, pore crush, shear deformation, damage, and spallation. The TOODY results are linked to AFD at points beyond the elastic radius, i.e., where rock deformation is purely elastic (refer to Figure 1).

A limiting factor in all of the calculations is computational zone size which, in turn, determines frequency resolution. The 1st order TOODY calculations employed either 20 m or 40 m zones in the region of interest that, depending on material sound speeds, yielded frequency resolutions in the range 1.5 Hz to 17 Hz. The 4th order AFD calculations used either 240 m or 480 m zones, resulting in frequency resolutions in the range 1.0 Hz to 3.0 Hz. Therefore, for the particular calculations being reported here, the limiting frequencies are determined primarily by the AFD calculations and are in the range 1 to 3 Hz. This masks the higher frequency characteristics of the nuclear explosion "signature" thus compromising to some extent an objective of this study.

General Problem Setup

Table 1 lists the source parameters and Table 2 lists the source geology for the TOODY calculations. Specific TOODY calculations are identified with the prefix "CTB" followed by the two ID numbers from the tables (e.g., CTB24 is for 64 kt @ 600 m depth in an alluvium/tuff layered basin). These number and letter designators are used in the Discussion of Results section.

Table 1

1st ID #	Source Energy and Depth(s)
0	No source energy
1	8 kt @ 300 m depth
2	64 kt @ 600 m depth
3	8 kt @ 600 m depth
4	12.8 kt @ depths of 300, 600, 900, 1200, 1500 m
5	13 sources at 300 m intervals, at 600 m depth along a horizontal from 0 to 3600 m
6	64 kt @ 1500 m depth

Table 2

2nd ID #	Source Geology
0	All crustal rock – no source basin – perfectly elastic
1	All crustal rock – no source basin
2	8.4 km diameter circular basin, 0.8 km deep composed of unsaturated alluvium
3	8.4 km diameter circular basin, 0.8 km deep composed of saturated tuff
4	8.4 km diameter basin as above but alluvium to 4 km depth, remainder tuff
5	8.4 km layered basin as above but all materials perfectly elastic

The fourth and fifth entries in Table 1 are not meant to represent realistic source configurations but rather extreme cases for determining the sensitivity of synthetic seismograms to such configurations. In Table 2, any material not noted as being perfectly elastic is allowed to deform inelastically according to the response properties deemed appropriate for that material. Unsaturated alluvium and saturated tuff are chosen because they represent materials very different from the crustal rock and also represent opposite extremes for stress wave propagation; alluvium is an efficient energy absorber and saturated tuff is an efficient medium for propagating energy away from the source into the elastic regime (App, 1993). Also, they are rock types found at the U.S. Nevada Test Site (NTS) that have been well characterized with respect to their dynamic response properties (App and Brunish, 1991)[1]. The basin geometry and TOODY-to-AFD linkage points are shown in Figure 2. The basin is bowl-shaped and its dimensions are somewhat arbitrary. The TOODY calculations are 2-D, axisymmetric and the explosion point is in the exact center of the basin. Because of the axial symmetry, the outgoing body wave is, to first order, spherically divergent.

Table 3 lists parameters for the regional propagation (AFD) calculations. AFD calculations are identified by the prefix SCM, NIL, or TLY, followed by the two digit number associated with the linked TOODY strong motion calculation, e.g., SCM24 is an AFD calculation that uses the simple crustal model linked to the TOODY layered basin calculation with a 64 kt source at 600 m depth

Table 3

ID	Description
SCM	Simple Crustal Model – 2 layers – crust and mantle
NIL	"simplified" path from Lop Nor to NIL seismic station in Pakistan
TLY	"simplified" path from Lop Nor to TLY seismic station in Inner Mongolia

The NIL and TLY paths are "simplified" in that both assume a flat Moho surface at 50.4 km depth. The NIL path crosses the large Tarim basin in Tibet and the TLY path crosses a smaller sedimentary basin in China. Figure 3 shows the TLY and NIL basins; for both the NIL and TLY paths, the depth and extent of the basins are taken from the Cornell Middle East/North Africa Project's online Profile maker, which also includes data from Eurasia. The explosion source is located at the end designated as "Lop Nor", however, the calculations make no attempt to model specifics of the Lop Nor Test Site. Previous calculations (App, et al., 1996) using only the AFD code and employing moment tensor representations for the source were made along these two paths as well as other selected paths in China. The results were in good qualitative agreement with observations for both explosions and earthquakes, thus forming the basis for using these models in this current study; i.e., there is a tie to reality. The previous calculations included the Moho topography, but subsequent work by Jones et al. (1997) indicate that the shape of the Moho in this part of China has a relatively minor influence on regional waveforms when compared with basin and topographic effects. The NIL and TLY paths were chosen for this study because they showed the more interesting effects in both the App and Jones studies, i.e., for an explosion source at Lop Nor, the signal recorded at NIL has an explosion-like appearance and the signal at TLY has an earthquake-like appearance (both measurements and calculations). Because of the significantly different effects the two paths have on the signal, they are logical first choices for use in evaluating the relative sensitivity of regional seismograms to various source and path configurations.

The regional paths are comprised of either two or three materials (cases TLY and NIL use three, SCM uses just the crust and mantle). Table 4 gives the elastic and anelastic properties of each. The sediment properties are used for the basins along the NIL and TLY paths. The Q values are somewhat loosely based on results of Minster (1980) combined with internal discussions with the Los Alamos CTBT R&D seismologists. The densities and sound speeds are based entirely on internal discussions (Warren, 1996).

---

[1] The App and Brunish (1991) reference addresses how well the models replicate observations. Actual physical and mechanical response properties for tuff and alluvium, which are very similar to what is used in this study, are available in App (1993), pages 12 and 13.

Table 4

Property	Sediment	Crust	Mantle
Density (kg/m3)	2800	2800	3300
P-Wave Vel (m/s)	5600	6100	8200
S-Wave Vel (m/s)	2500	3500	4700
Qp	200	500	1000
Qs	53	219	439

All TOODY calculations use a rectangular computational grid. The zones in the source region, and extending out just beyond the AFD linkup points shown in Figure 2, are either 20 m or 40 m squares depending on the particular problem being run. With increasing distance from the source and AFD linkup points, the zones gradually become larger in order to minimize computational time and memory usage. TOODY does not support "absorptive" boundaries, therefore, the mesh must be sized large enough such that reflections from the mesh boundaries do not interfere with the signal at the AFD linkup points. The boundaries are at either 35000 or 55000 m range (both horizontal and vertical), again, depending on the particular problem being run. There is a zone size discontinuity at 2400 m depth where the radial (horizontal) dimension of the zones abruptly doubles in size from the zones immediately above that depth. This "numerical discontinuity" produced a small, non-physical reflection that is mentioned later in this report.

TOODY is a 1st order code. The maximum frequency of a simulation is determined from the criterion of 10 computational zones per resolved wavelength, and is governed by the wavespeed of the material. For example, using a 20 m zone size and for the wave speeds given for crust in Table 4, the maximum P-wave frequency resolved is about 30 Hz and the maximum S-wave frequency is about 17 Hz.

The AFD code does support absorptive boundaries, therefore, the mesh need not be much larger than the "region of interest". AFD's drawback, however, is that all zones must be square and of the same size. In this study, zone sizes of either 240 m and 480 m (on a side) were used, depending on the specific problem being run. For near-regional calculations the absorptive boundaries were at 639.84 km radial distance and 76.8 km depth. For the regional calculations the absorptive boundaries were at 1700.16 km radial distance and 76.8 km depth.

AFD is a 4th order (in space) code. The maximum frequency of the simulation is determined by the criterion of 5 computational zones per resolved wavelength. For example, using the 240 m zone size and for the wavespeeds given for crust in Table 4, the maximum P-wave frequency resolved is about 5 Hz and the maximum S-wave frequency is about 3 Hz.

Discussion of Results

It was mentioned in the Introduction Section that one potential use of this study is as a template for further study. Not all of the possible combinations of calculations listed in the tables have been conducted; in particular, the lower yield 8 kt calculations experienced numerical problems related to the particular overburden scheme used in TOODY. Ideally, in problems that include gravity, the initial state of stress must be preset to a condition of complete equilibrium. This is a difficult problem for cases with large lateral changes in density such as exist in the source basin calculations. The particularly scheme used in TOODY for addressing the non-equilibrium problem was not precise enough for the 8 kt calculations, i.e., the motions due to non-equilibrium effects were comparable in amplitude to the seismic signal. For this reason, the results of the 8 kt basin calculations are not included in this report. Also, the TOODY calculation with horizontally-aligned, multiple sources (Table 1, item #5) was not linked to AFD for propagation to near-regional distances; this was the only TOODY calculation run in X-Z (plane strain) geometry and to include it would have expanded the scope of the study beyond what was considered practical at this

time. It would be useful to include the calculation as part of a general sensitivity study that uses X-Z geometries for both close-in and regional calculations.

As alluded to in the above mesh descriptions, the TOODY-AFD linked calculations are organized into two groups: a) 3 Hz near-regional simulations out to 600 km and b) 1 Hz regional simulations out to 1700 km. The near-regional calculations employ the 240 m zone size and the regional calculations use 480 m zones.

a) Near-regional calculations - 3 Hz resolution

In this series the TOODY calculations are made for a simple half-space assuming the density and sound speeds presented in Table 4 for crust; there are no other rock types. The material is assumed saturated (no trapped air voids) and has an unconfined shear strength of about 3 Mpa (30 bars) and a maximum shear strength (under very high confining pressure) of 700 Mpa (7 kb). These strengths are chosen to allow substantial shear failure in the vicinity of the source. The model can be thought to represent a highly fractured but dense rock that is relatively weak near the ground surface but gains considerable strength with increasing depth. At 600 m depth, the shear strength of the in-situ rock is about 15 Mpa (150 bars). The effects of gravity are included in the calculations and, except where noted, shear failure around the explosion point and surface spallation and recompaction are allowed to occur.

There are four TOODY calculations in this series:

CTB21 - 64 kt source at 600 m depth;

CTB20 - identical to CTB21 except that the rock is infinitely strong;

CTB61 - like CTB21 but the energy source is at a depth-of burial (DOB) of 1500 m;

CTB41 - five 12.8 kt sources at DOBs of 300, 600, 900, 1200, and 1500 m (for a total energy yield of 64 kt).

The objective is to determine the sensitivity of the near-regional signal to rather extreme variations in source conditions. For 64 kt, the 600 m DOB used for CTB21 is adequate for containing underground most, if not all, of the radioactive products produced by the nuclear explosion[2]; this case can be considered the "baseline" case against which others should be compared. CTB61 is very much overburied for containment. Figure 4 shows the x (radial) particle velocity at a TOODY-AFD linkup point at a surface location 4320 m distant from surface ground zero (SGZ) for each of the four cases. Figure 5 shows the vertical velocities at the same locations. Because CTB20 is in an infinitely strong medium, its amplitude is diminished from the finite-strength calculation CTB21. It also is of higher frequency and generates a relatively weak surface Rayleigh wave (Rg). The most outstanding difference between CTB61 (greater DOB) and CTB21 (normal DOB) is the Rg; the Rg is much stronger for the shallower-DOB case. Not surprisingly, the multiple source calculation (CTB41) is intermediate between CTB21 and CTB61 with regard to surface wave generation. For CTB41, the initial P-wave is quite coherent at the edit points selected for Figures 4 and 5, but, at edit points more directly beneath the sources, the signal arrivals present themselves as distinctly separate pulses (not shown). Despite the fact that its total energy is 64 kt, the waveform for CTB41 shows much less amplitude than either CTB21 or CTB61; however, this

---

[2] In most settings the event would be fully contained, but in certain rock types such as highly jointed or brittle rocks there might be some leakage.

may be partly an artifact of the manner in which energy is deposited into the rock in these calculations, and not a real physical effect.[3].

Figures 6 and 7 show radial and vertical velocities at the same horizontal range as above but at a "receiver" depth of 1920 m; this also is one of the TOODY-AFD linkup points. Again, one notes the diminished amplitude and higher frequencies associated with the CTB20 infinite strength case relative to the CTB21 finite strength case. The pS shear wave is about equally strong (in a relative sense) for all four cases; this suggests that spall may play only a minor role in its development since CTB20 allowed no spall. The pS for CTB41 is slightly broader than for the other cases because of the distributed source. From evidence that will be discussed later in this report, there is some indication that we are seeing some S*[4] in the CTB21 calculation. The conditions for it are about right in that the strength of the S* phase is dependent on a DOB/wavelength relationship (Gutowski, et al., 1984) for which CTB21 is well suited.

Figure 8 shows x-z shear stress and mean stress (pressure) for the same edit points shown in Figures 6 and 7. A comparison of pressure and x-z shear allows one to separate the shear stresses that develop due to outward, spherical expansion of a compressional body wave from shears that develop from other sources such as P to S conversion at the free surface. Shear stress in the absence of a change in mean stress implies pure shear. Such is the case with pS; all four cases develop substantial shear stress for pS with no significant change in mean stress; S* for CTB21 is another example.

Figures 9 and 10 show "snapshots" of the particle velocity field at 740 ms for the four cases. They show the close-in development of the various phases that eventually get transmitted to regional distances. All four cases develop a strong pS shear wave from the free surface, in fact, the pS for the CTB41 multiple-source calculation shows a remarkably coherent pS wave considering the fact that the source was distributed over a distance of 1200 m. A much broader, lower amplitude pS wave was expected for this case; instead it appears that the rather arbitrarily chosen source separations caused reinforcements leading to a highly coherent pS phase. The pP appears to be strongest for the CTB61 (overburied) case. It appears weaker for CTB20 (no spall) suggesting that spall plays a role in the strength of that phase. The pP phases for the multiple-source CTB41 case cannot be clearly identified in the plots. A "false reflection" is labeled on the vector plot for CTB20 but it also is noticeable for the other cases as well. This is a reflection from the zone-size discontinuity at 2400 m mentioned in the mesh descriptions. Its amplitude is quite small relative to the other phases, therefore, we do not believe that it poses a really significant defect. There is a hint of the S* shear body wave in the CTB21 calculation. At these close-in ranges it is interfered with by one or more other phases, possibly including some Rg and/or shears developed by asymmetrical cavity oscillations. As mentioned earlier, S* should be better developed in the relatively shallow CTB21 calculation than in the others, and this appears to be the case. At significantly greater ranges (after linkage to AFD) the S* is more easily seen as a single, distinct phase (not shown), however, it is weak.

Figure 11 shows the regions of material failure for CTB21, CTB61, and CTB41 (there is no material failure for CTB20). These are to provide the reader with some appreciation of the extent of failure being addressed in this study. The extent of rock failure (inelastic deformation) is rather modest when compared to many events conducted at, for example, the NTS; therefore, this study is not addressing "worst cases" in this regard. For CTB41, surface spall is suppressed due to

---

[3] The source energy can be introduced in a variety of ways with the TOODY code. In many applications the energy often is simply deposited into a volume of rock that represents the volume expected to be vaporized in a nuclear explosion, therefore, the greater the energy, the larger the volume into which energy is deposited. It has been found that this results in fairly consistent energy coupling from case to case. Because absolute amplitude of the signal is of minimal interest in this particular study, energy is deposited into volumes considerably in excess of the "vaporization" volumes and no real attempt has been made to assure that percent energy coupling is consistent from one case to another.

[4] S* are pure shear body waves caused by the interaction of shallow, explosion produced stress waves with the free surface.

interference between successive stress waves approaching the free surface, however, this same interference apparently resulted in a quite coherent-appearing pS signal. It is likely that different spacing and/or timing could result in enhanced spall, and perhaps less coherent pS, but calculations to find such a configuration were not performed.

The results of the four TOODY calculations were linked to AFD for calculations extending to 200 sec in time and 600 km surface range. In these particular AFD calculations, there are no topographic features or basins to break up the signal. The AFD model consists of just two layers, the crust and mantle. Physical properties of the crustal rock are the same as used for the TOODY calculations and are listed in Table 4, the only difference being that the TOODY calculations are without Q attenuation. The reader is reminded that the zone size of the AFD calculations preclude meaningful frequencies above 3 Hz despite the fact that the TOODY calculations for this series are good to almost 20 Hz. For numerical reasons alone, therefore, some details from the close-in calculations are lost in propagation to near-regional distances.

Prior to linkage from TOODY to AFD the signals were processed with a 4 Hz low pass filter. Figure 12 shows a comparison of filtered and unfiltered waveforms at the x = 4320 m, z = 1920 m edit point. Most of the main phases are captured, but the relative amplitudes between phases are moderately effected by the filtering. The signal for the CTB20 purely elastic case is most strongly effected because of its overall higher frequency content.

The AFD generated seismograms are band pass filtered 0.1 to 3 Hz. Figure 13 shows vertical (z) component seismograms along the surface from 100 to 600 km for the CTB21 (normal DOB) calculation. The Rg is by far the dominant phase. Recall that there is nothing along the path to break up or convert the Rg to other phases. Figure 14 shows a detail of the z-component of Rg at 600 km surface range for each of the four calculations. The scales are fixed to $\pm 3 \times 10^{-6}$ m/s. The results are consistent with those from the close-in calculations, namely the Rg is strongest for the normally-buried CTB21 case and weakest for the infinite-strength CTB20 case, although adverse filtering effects (Figure 12) have some bearing on the CTB20 results. There are no substantial differences in frequency content or pulse duration. Figure 15 compares the waveforms for the four cases prior to the arrival of Rg (maximum time of plot is 183 sec, Rg arrives at 184 sec). The refracted P and repeatedly reflected Pg arrivals are clearly evident, however there is no indication of Lg. Absence of Lg is not surprising since the "China-like" velocity model used in these calculations is poorly suited for crustal trapping of shear waves generated by P to S conversion along the free surface; i.e., the P-wave velocity of the crust (6.1 km/s) is considerable greater than the S-wave velocity of the mantle (4.7 km/s). Using a computer code very similar to the AFD code, Xie and Lay (1994) demonstrated that, for a horizontally layered crust, the ratio of source region P-wave velocity to mantle S-wave velocity is a critical factor in the crustal trapping of shear energy and the formation of Lg[5]. Even if the crust and mantle velocities were adjusted to be more conducive to shear wave trapping in the current calculations, we doubt that there would be much difference in the relative strengths of Lg between the four cases since the close-in pS phase is about the same for all. The S* phase should become more easily trapped in the crust since the ratio of S-wave velocities between crust (3.5 km/s) and mantle (4.7 km/s) are the critical velocities for trapping these shear body waves. Rays with angles of incidence greater than 48 degrees will be critically reflected, however, there is no sign that S* is contributing significantly to the Lg in these calculations. Regarding the Rg, the difference in geometric attenuation between Rg and Pg (which works in favor of Rg) apparently is more influential than the differences in Q for the two phases (which works in favor of Pg), resulting in a strongly dominant Rg at near-regional and regional distances. This affirms the need to include Rg scattering from such features as basins and mountains for realistic simulations.

---

[5] The horizontal component of velocity of the free-surface generated shear wave (pS) associated with an explosion travels at the compressional (p) sound speed, not the shear sound speed, and therefore is not as readily trapped within the crust as is (for example) an earthquake generated shear wave. To put it another way, there are no post-critical reflections for pS and therefore leakage to the mantle occurs.

Figure 16 shows an expansion of the refracted P first arrival portion of the 600 km seismograms. Even in this phase, which should undergo the least modification during transmission to near regional distances, there is little to discriminate between the four cases.

For the four cases examined, the main and obvious conclusion to be drawn is that at frequencies 3 Hz and below, and for the crudely China-like properties used, spall, shear failure, source depth, and source configuration do not substantially alter the near-regional signal. A question remains as to how the signal is influenced at higher frequencies and/or with different crust and mantle velocity and Q structures.

b) Regional Calculations - 1 Hz resolution

The foregoing discussion dealt with very simple geologic settings for both the source and regional wave propagation. The next series of calculations add some complications to the source geology and the paths, but overall the settings remain highly idealized. Eight calculations are discussed; more were made but they add nothing substantial to the findings, and some were made simply as numerical check cases for confidence building. The eight calculations are described below:

SCM21 - employs the same source and crustal descriptions used for CTB21. The TOODY calculation is the same calculation used for CTB21 but the waveforms at the AFD linkup points are processed with a 2 Hz low pass filter rather than 4 Hz.

SCM24 - employs the same regional path description used in SCM21 but the 64 kt source is located at 600 m depth in the tuff portion of a two layer structural basin described in the problem setup section (see Figure 2). The sound speeds for the alluvium and tuff sections increase linearly with depth. For the alluvium, the P and S-wave velocities at the free surface are 1191 m/s and 600 m/s respectively and at 400 m depth are 1691 m/s and 1233 m/s respectively. The P and S-wave velocities for the tuff at 400 m depth are 2210 m/s and 1233 m/s respectively and at 800 m depth are 2802 m/s and 1564 m/s respectively.

SCM22 - employs the same regional path description used in SCM21. Source is 64 kt at 600 m depth in a basin with dimensions as shown in Figure 2. The entire basin is composed of unsaturated alluvium. The P and S-wave velocities at the free surface are 1191 m/s and 600 m/s respectively. At 800 m depth, the P and S-wave velocities are 2191 m/s and 1104 m/s respectively. From the free surface to the bottom of the basin at 800 m, the P-wave velocity gradient is constant at 2.5 m/s per meter depth. An all-alluvium basin is an extreme case for evaluating non-linear effects, but similar settings could exist in certain parts of the world (notably the NTS).

SCM23 - employs the same regional path description used in SCM21. Source is 64 kt at 600 m depth in a basin with dimensions as shown in Figure 2. The entire basin is composed of saturated tuff. The P and S-wave velocities at the free surface are 2210 m/s and 1233 m/s respectively. At 800 m depth, the P and S-wave velocities are 3790 m/s and 2114 m/s respectively. From the free surface to the bottom of the basin at 800 m, the P-wave velocity gradient is constant at 1.975 m/s per meter depth.

NIL21 - employs the same source region description as SCM21 but the regional path has the NIL configuration (large sedimentary basin - see Figure 3).

NIL24 - combines the SCM24 source region configuration (layered basin) with the NIL path.

TLY21 - employs the same source region description as SCM21 but the regional path has the TLY configuration (small sedimentary basin - see Figure 3).

TLY24 - combines the SCM24 source region configuration with the TLY path.

9

For the calculations involving source basins (22, 23, and 24 series), the source is located in material with P-wave velocities less than the mantle S-wave velocity, but the low velocity material extends no further than the boundaries of the basin. Also for 22, 23, and 24, the zone size for the TOODY calculations is increased from 20 m (used for 21 series) to 40 m. This, combined with the lower near-surface sound speeds, limits the frequency resolution to a maximum of 1.5 Hz in cases involving alluvium.

Figures 17 and 18 show the x (radial) and z (vertical) particle velocities at the 4320 m surface range edit point for the 21, 22, 23, and 24 series TOODY calculations. The 21 series (no source basin) waveforms are the same as shown in Figures 4 and 5 but with expanded time scales to match those of the basin calculations. Figures 19 and 20 show x and z velocities respectively at the 1920 m depth edit point (4320 m horizontal range). Figure 21 shows the mean stresses and x-z shear stresses for the same four calculations at the 1920 m depth point. The most notable characteristic of the basin calculations is the pattern of reverberations that occur because of interlayer and basin edge reflections. The basin calculations were carried out to problem times of 18 sec in order to capture the majority of these reverberations. Although the first pulses (P-waves) are somewhat difficult to see in these plots, their periods are considerably longer than for the 21 series, no-basin calculation; also, the amplitudes are lower. The observed broadenings and amplitude reductions are due largely to the more severe inelastic deformation that occurs for rock types in the basin.

The coherency and relatively high amplitudes of the reverberations are attributed to the symmetry inherent in the 2-D treatment. In a "real-world" basin setting there would be much greater scattering and the reverberations would be less obvious, but they would still occur. For the purposes of this study, we consider the coherence of the reverberations to be a positive factor since they can be easily identified at regional distances. For SCM22 (all-alluvium basin) and SCM24 (layered basin) the reverberations continue past 18 sec; however, in order to keep total computing run times within practical limits, the calculations were terminated at 18 sec. The reverberations appear to have a fundamental period of about 1.5 sec and we believe, but have not proven, that they would be relatively insensitive to details of inelastic response or special source configurations discussed above in connection with the near-regional calculations. In comparing the mean stress and x-z shear stresses in Figure 21, there appears to be a substantial amount of shear energy associated with the reverberations, but it is not all shear.

During the investigations there was some concern that the amplitude and duration of the calculated reverberations was unrealistic because TOODY calculations do not include seismic Q. A special AFD calculation (not shown) was performed using a source basin almost identical to that used in the TOODY layered-basin model, but which included the seismic Q values for sediment given in Table 4; the results were very similar to the TOODY results with respect to relative amplitude and duration of the reverberations.

Figure 22 shows "snapshots" of the particle velocity field at 1.4 and 2.7 sec for the TOODY 24 series layered basin calculation. The plots are essentially uninterpretable because of the extreme complexity of wave interactions. Plots of Divergence and Curl for the velocity field were made (not shown) that confirm the generation of significant shear within the basin, some of which gets transmitted outward with each reverberation.

A note of caution regarding the linkage of the TOODY calculations to the low frequency AFD calculations, especially with regard to the 21 series (no-basin) calculation. As mentioned before, the TOODY signals are low pass filtered prior to linkage, therefore, some of the details of the waveforms are lost. This problem is potentially more severe than it was for the higher frequency near-regional cases since the signals for the regional calculations were processed with a 1.5 Hz low pass filter (2 Hz for SCM21). Figure 23 shows a comparison between the filtered and unfiltered signals at the 1920 m depth point (x=4320 m). The 21 series source is the most severely effected since its initial frequency content is quite high. The basin calculations are minimally effected because the initial pulse is of lower frequency for the weaker basin rocks and the basin reverberations are of low frequency.

Figures 24 and 25 show the evolution of the seismic waves at the surface and at 20 km depth respectively for the SCM21 (no source basin) case. Along the surface the Rayleigh wave is so dominant that scaling the plots to its amplitude causes the other phases to be nearly invisible. At 20 km depth, all of the important phases are observable. In Figure 25 straight lines are drawn to roughly correspond to the first arrivals of the various phases; they do not match perfectly with each arrival because the seismograms are not always centered vertically in the boxes. The apparent velocities are consistent with the input velocities of the problem. The weakness of the Pn is attributed to the absence of a velocity gradient in the mantle. The line identified as Rg in Figure 25 is taken directly from the Rg arrivals along the surface in Figure 24. They match exactly with the arrival of the largest amplitude portion of the signal and, therefore, we believe that this is a subsurface expression of the surface wave (recall that this is a single-velocity crust). A special dispersion analysis done by Patton (1997) further supports this interpretation. Over most distances the Lg (which we will designate as the portion of the wavelet between the Lg and Rg lines) is of an amplitude comparable to the Pg, tending to become more dominant with increasing distance. Figures 26 and 27 are for the TLY21 case (TLY path, no source basin). The only significant difference between it and SCM21 is the broadening of the Rayleigh wave train due to scattering in the small basin along the TLY path (Figure 3). The original study that addressed various paths in China (App, et al, 1996) found good agreement between calculations and measurements along the TLY path, but at the time of that report the physical processes had not yet been identified. Subsequently, Jones, et al. (1997) determined that the "earthquake-like" appearance of the seismogram at TLY probably is due to creation of Rg at the source-ward basin edge combined with low attenuation in the crust and the absence of significant topography for converting the Rg wave to other phases. The strong, late-arriving signal at TLY that makes it appear "earthquake-like" is not Lg but rather Rg. This study supports the Jones, et al. findings. Figures 28 and 29 are for the NIL21 case (NIL path, no source basin). The results are quite different from those of either SCM21 or TLY21. Note that the Rg beyond 1000 km is delayed and considerably attenuated compared to the SCM and TLY cases. The Lg and the Rg are now well separated in time but it is difficult to determine if the duration of the Lg is greater because in the SCM and TLY cases the trailing portion of Lg and the beginning of Rg appear to run together. Jones determined that the increased Lg and decreased Rg amplitudes are probably due to a combination of P to S conversions along the sediment-crust boundaries of the large Tarim Basin (Figure 3), shear reverberations within the basin, and attenuation of the Rg within the low Q materials of that basin. There appears to be a fundamental differences in how the regional signal is modified by small vs. large basins and the magnitude of the differences probably is highly dependent on the sediment Q values.

The purpose of the current study is not to replicate the results of Jones but rather to determine if seismograms generated from different source conditions and configurations are impacted differently by the basins, and to determine the relative importance of close-in vs. regional path effects. Figure 30 shows a detail of the z-component of Rg at 1350 km for the four cases that have no complications along the regional path (the SCM series). Figure 31 shows the same four cases with scales adjusted to allow comparison of the Pg and Lg amplitudes. A significant result is that the relative amplitudes between phases do not appear to be much different for the four cases, this despite the wide disparity in source materials. We are not, however, seeing the entire Lg packet because of interference with the Rg. Even the absolute amplitudes are not very different for the three basin calculations. The caution here, however, is the same one mentioned earlier; i.e., no special cautions were made in the introduction of energy into the problem to assure consistent energy coupling; also, the TOODY zone sizes were probably too large to adequately capture peak amplitudes. It would be possible to perform the calculations in such a way to address the detection (amplitude) issue, but that is beyond the scope of the current study.

Figure 32 shows the path effects using both the 21 (no basin) and 24 (layered basin) source descriptions. Figure 33 is the same as Figure 32 but with fixed scales. For SCM24 and TLY24, the effect of conducting an underground nuclear explosion within the basin is to broaden the Rg and decrease its amplitude relative to earlier phases, but the general character of the signal remains the same. For NIL24 there is no Rg broadening and the Rg amplitude is reduced considerably relative to the other cases, and relative to the earlier phases. There is no significant change in the

duration or character of the Lg between the NIL21 and NIL24 cases, the only cases in which the entire Lg packet is visible. Figures 34 and 35 are analogs to Figures 32 and 33 except they show the x (radial) component of motion. From a discrimination standpoint, the important result is that for the idealized regional paths chosen for this study, and at the frequencies addressed, path effects very much dominate over source effects.

Summary

Under the assumptions made in this study, our tentative conclusions are that: 1) spall, non-linear deformation, and depth-of-burial do not substantially influence the near-regional signal and 2) the source region influences waveforms relatively little compared to the effects due to basins along the regional path.

Caveats associated with the above conclusions are: 1) a very small number of cases are treated, 2) there are limitations on the frequency resolution, 3) the crust-mantle velocities used are such as to discourage a strong Lg signal for explosions, 4) the effect of varying Q was not investigated, 5) the basin configuration chosen for the close-in calculations is very highly idealized and chosen more for computational convenience than anything else (although it did appear to represent a relatively severe case of signal alteration).

While the results shown here are encouraging from the standpoint of discriminating nuclear explosions from earthquakes, they are not encouraging with respect to discriminating underground nuclear detonations from, for example, mine blasts. Under our current limitation to low frequencies, some characteristics unique to nuclear explosions (and probably mine blasts as well) simply cannot be seen at regional distances; however, the study does indicate that even low frequency signals such as basin reverberations would not necessarily be recognized as such, especially if there are complications along the regional path.

Recommendations for Further Work

In this study, various source configurations caused relatively minor perturbations in the regional waveforms when compared to the influence of sedimentary basins along the regional path. We should extend this study to determine if the same holds true at higher frequencies. We currently have no practical means of doing this, however, some insights can be gained if we restrict ourselves to flat layers along the regional path and link strong motion calculations to a reflectivity-based code such as was described in the General Approach section. If high-frequency close-in effects have no more influence on regional seismograms than the low-frequency CTB and SCM calculations, it would probably be safe to conclude that inclusion of complications along the regional path would not change that result.

In order to make the conclusions of this study less tentative for the low frequency cases, we recommend a modest extension of the work to include different crustal velocity structures and other values of seismic Q. For some of this, the current TOODY waveforms can be reused.

We recommend continued low-frequency finite difference work that addresses path effects alone (without strong-motion linkups) since they were found to be dominant over source effects at the lower frequencies.

We suggest that future work can build on the approaches and results presented here. With forthcoming improvements in the AFD code (performed under funding outside CTBT), higher resolution calculations should be possible with that code in the foreseeable future and some of the AFD calculations that include basins (or, for that matter, surface topography and Moho structure) can be repeated at higher resolution. Some of the TOODY calculations are already at higher resolution and linkup points are arranged for linking to AFD zones as small as 120 m. To go to resolutions generally higher than 6 Hz requires that the strong motion calculations be redone with more finely-spaced edit points and, in some cases, finer zoning.

Acknowledgments

We believe modeling is crucial to the CTBT R&D program. It is the opinion of the authors that only a very limited understanding of the physical basis for discrimination is possible through empirical approaches alone and, without a substantial modeling effort, weaknesses and pitfalls in discrimination methods may not be identified until after treaty implementation. We are hopeful that the seismic modeling efforts for CTBT R&D can be supported at a level adequate to do the task in a timely manner.

References

F. N. App and W. M. Brunish, *Stress Wave Calculations of Four Selected Underground Nuclear Tests: MERLIN, HEARTS, PRESIDIO, MISTY ECHO*, Los Alamos National Laboratory Report EES-NTC-91-03, Jan. 1991.

F. N. App and W. M. Brunish, *Modelling Surface Motion and Spall at the Nevada Test Site*, Los Alamos National Laboratory report LAUR-92-500, Jan. 1992.

F. N. App, *Sensitivity of the Close-in Seismic Source Function to Rock Properties*, Los Alamos National Laboratory report LAUR-93-1884, May 1993.

F. N. App, R. J. Bos, T. N. Dey, E. M. Jones, J. R. Kamm, and S. R. Taylor, *Examining Near-source Effects in the Far Field*, Proceedings of the 17th Seismic Research Symposium, 12-15 September, 1995.

F. N. App, R. J. Bos, and J. R. Kamm, *Synthetic Seismograms at regional Distances for May 1995 Earthquake and Explosion Sources in Western China*, Proceedings of the 18th Annual Research Symposium on Monitoring a Comprehensive Test Ban treaty, 4-6 September, 1996.

T. C. Bache, S. M. Day, and H. J. Swanger, Rayleigh wave synthetic seismograms for multi-dimensional simulations of underground explosions, *Bull. Seism. Soc. Am..*, 72, 15-28, 1982.

T. N. Dey & J. R. Kamm, *User's Guide to SMC-123*, Los Alamos National Laboratory unpublished report, 1994.

L. A. Glenn, *Modeling the Explosive Source Region: An overview*, in Proceedings of the Numerical Modeling for Underground Nuclear Test Monitoring Symposium, eds. S. R. Taylor & J. R. Kamm, Los Alamos National Laboratory Report LA-UR-93-3839, 1993.

P. R. Gutowski, F. Hron, D. E. Wagner, and S. Treitel, S*, *Bull. Seism. Soc. Am.* 74, 61-78, Feb. 1984.

E. M. Jones, F. N. App, and R. J. Bos, *The Effects of Major Structural Features on Seismic Waveforms Traversing Paths in Western China*, Los Alamos report in preparation, July 1997.

J. R. Kamm and R. J. Bos, *Comparison of Chemical and Nuclear Explosions: Numerical Simulations of the Non-Proliferation Experiment*, Los Alamos National Laboratory report LA-12942-MS, June 1995.

J. R. Kamm, R. J. Bos, E. M. Jones & N. Cheng, *Modeling of Regional Seismograms due to Explosion Sources with 2-D and 3-D Finite Difference Calculations*, presented at American Geophysical Union Fall Meeting, San Francisco, CA, December 12, 1995, LA-UR-95-3072.

J. R. Kamm, R. J. Bos & E. M. Jones, *User's Guide to AFD v. 1.0*, Los Alamos National Laboratory report LA-UR-96-853, March, 1996.

Los Alamos National Laboratory, *The RAGE Page*, User Manual Website address: http://garner.lanl.gov/rageman/noframes_toc.html, 1997.

K. L. McLaughlin, T. G. Barker, S. M. Dat, B. Shkoller, and J. L. Stevens, *Effects of depth of burial and tectonic strain release on regional and teleseismic explosion waveforms*, S-Cubed, LaJolla, California, AFGL-TR-88-0314, 115pp, 1988.

J. B. Minster, Anelasticity and Attenuation, in *Physics of the Earth's Interior, Proc. Enrico Fermi Int. School Physics*, eds. Dziewonski & Boschi, 551.1 v295s, North Holland, 1979.

H. J. Patton, private communication, July 1997.

N. Rimer, H. E. Read, S. K.Garg, S. Peyton, S. M. Day, and G. A.Hegemier, *Effects of Pore Fluid Pressure on Explosive Ground Motions in Low Porosity Brittle Rocks*, DNA Report TR-85-245, 1984.

B. W. Stump, D. C. Pearson, and R. E. Reinke, *Source Comparisons between Nuclear and Chemical Explosions Detonated at the Rainier Mesa Nevada Test Site*, Los Alamos National Laboratory report LAUR-94-4073, Dec. 1994.

J. W. Swegle, *TOODY IV - A Computer Program for Two-dimensional Wave Propagation*, Sandia National Laboratory report SAND-78-0552, September, 1978.

S. R. Taylor and F. N. App, *Representation Theorem Coupling of Numerical and Wave Propagation Codes for the Generation of Synthetic Seismograms*, Los Alamos National Laboratory report LAUR-94-2194, June 1994.

R. G. Warren, private communication, Feb. 1966

X. Xie and T. Lay, The Excitation of Lg Waves by Explosions: A Finite-Difference Investigation, *Bull. Seism. Soc. Am.* 84-2, 324-342, Apr. 1994.
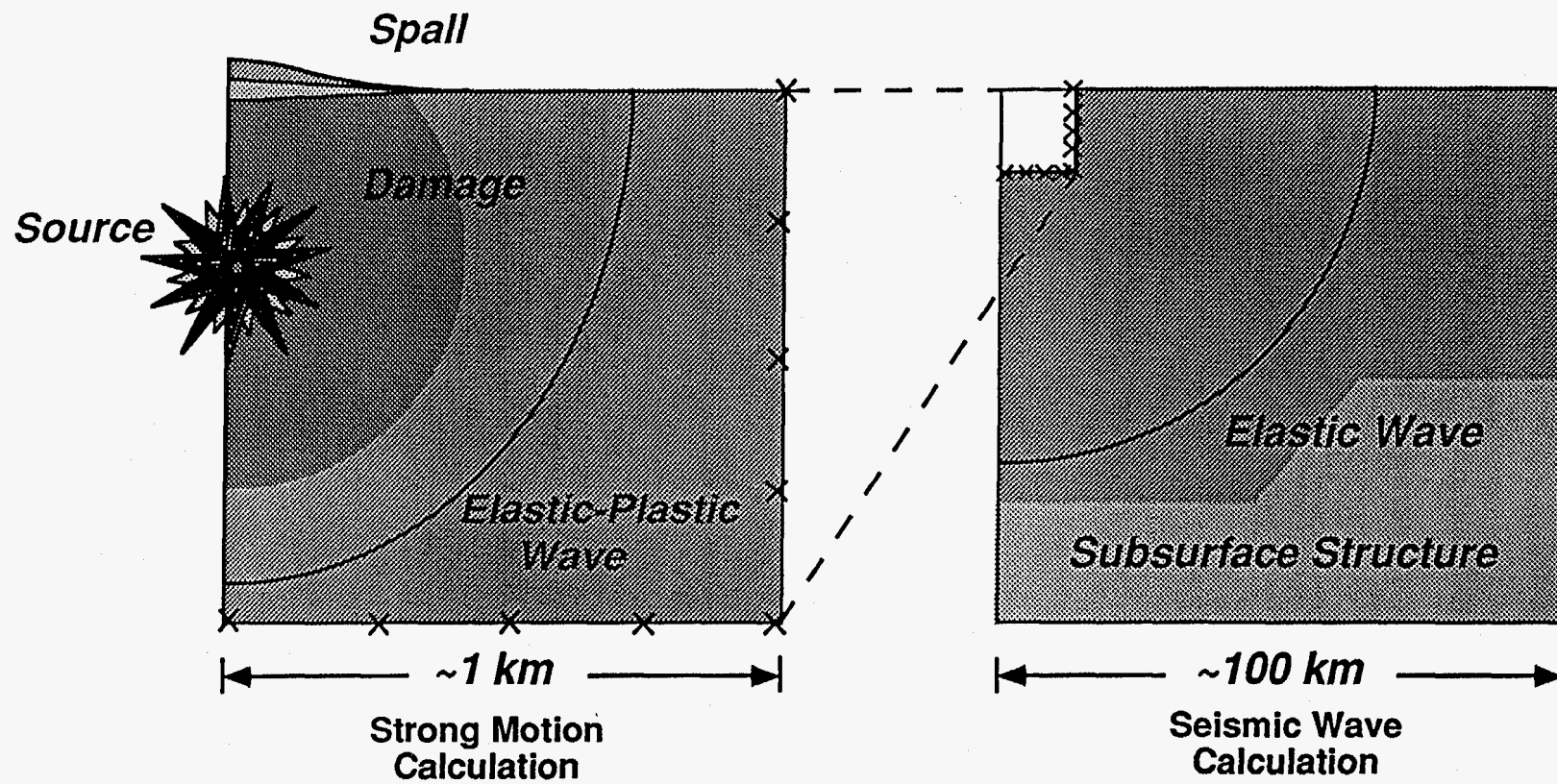
Fig. 1 Code coupling procedure for linking the results of a strong motion, weapons effects, calculation that includes all of the important physics of an underground nuclear test in any particular configuration, to an elastic wave code for propagating the signal to regional distances. In this way, we are able to study the relationship between radiated seismic signals and the details of the nuclear source.
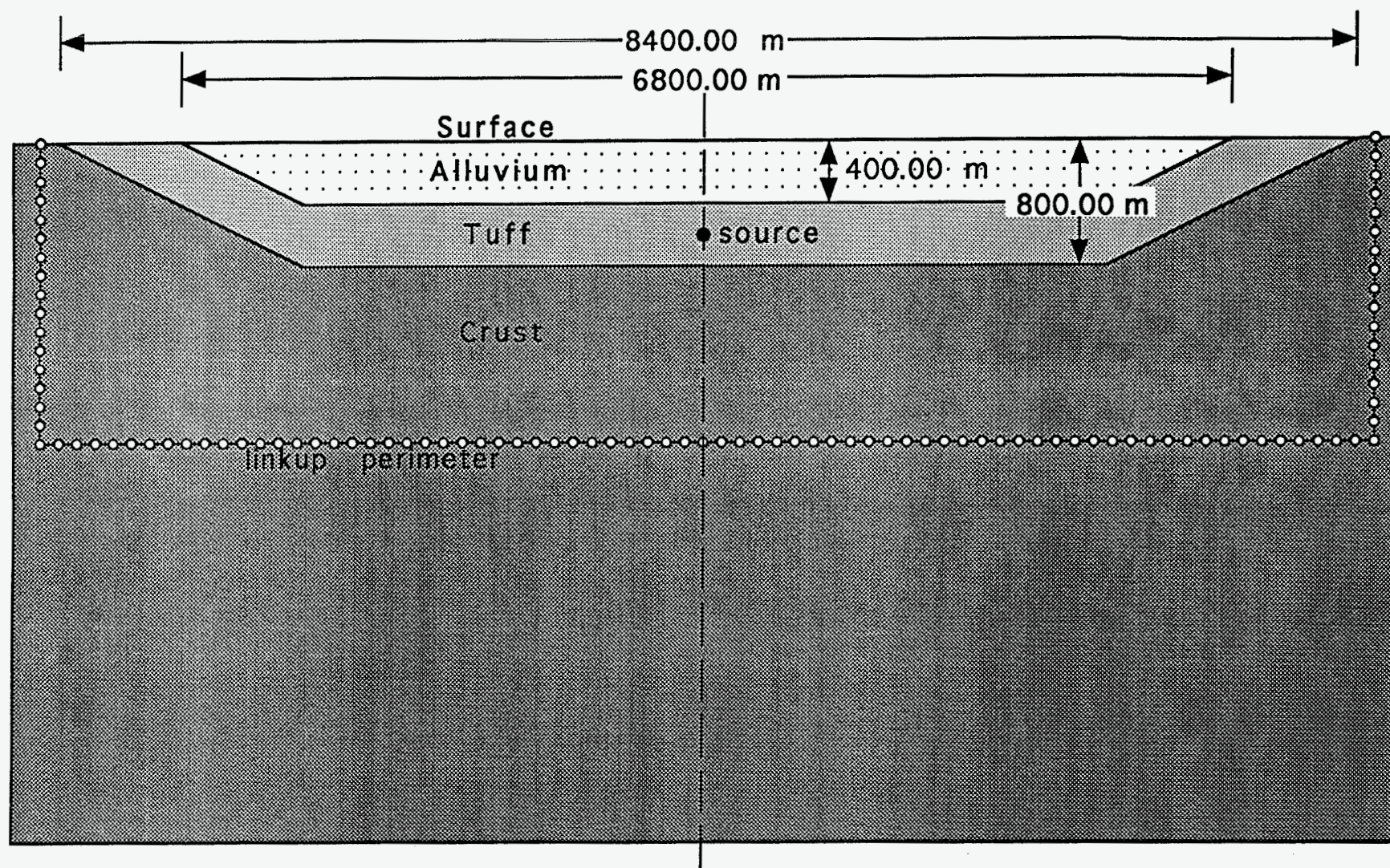
Fig. 2 Schematic of layered source basin showing the TOODY-AFD linkup perimeter.
The center line is an axis of rotation so only half of the model is actually calculated.

Fig. 3 Basin profiles (light areas) for the Lop Nor to TLY path (upper) and Lop Nor to NIL path (lower); 25:1 vertical exaggeration.
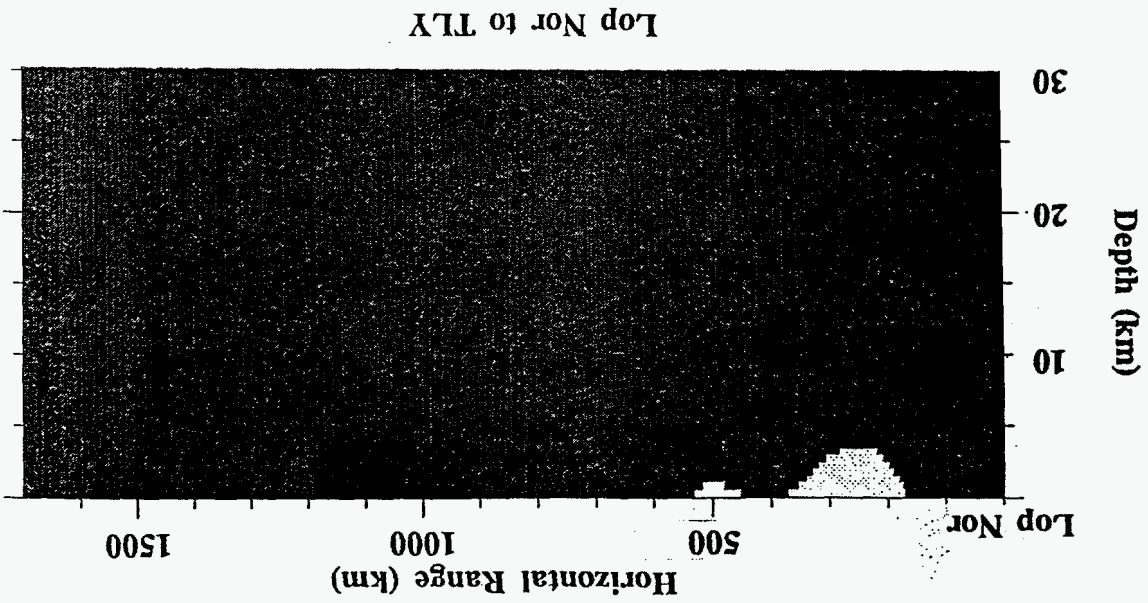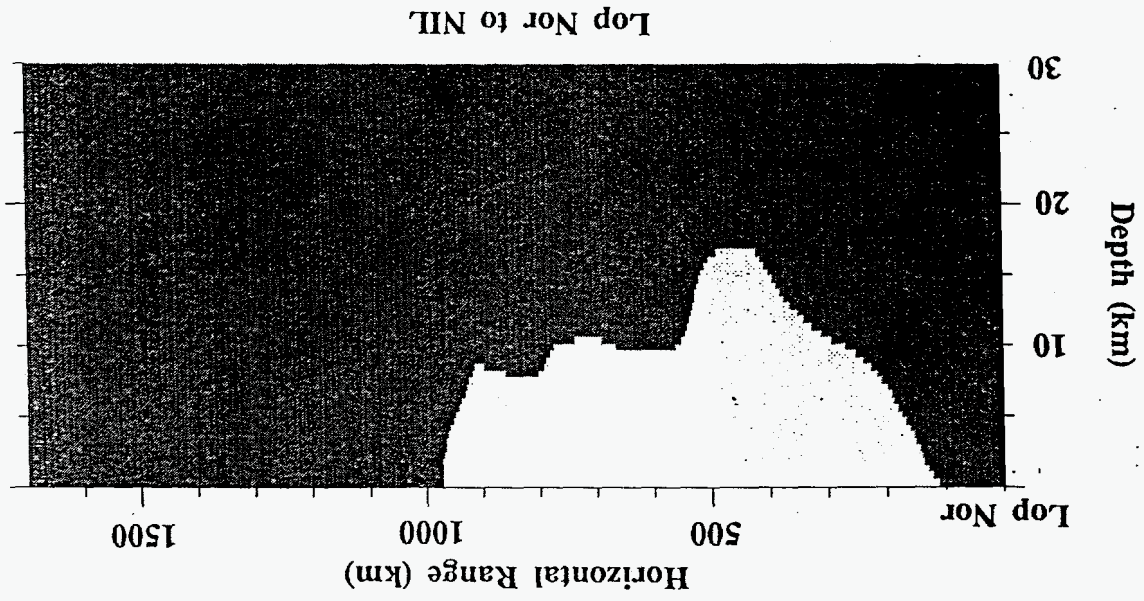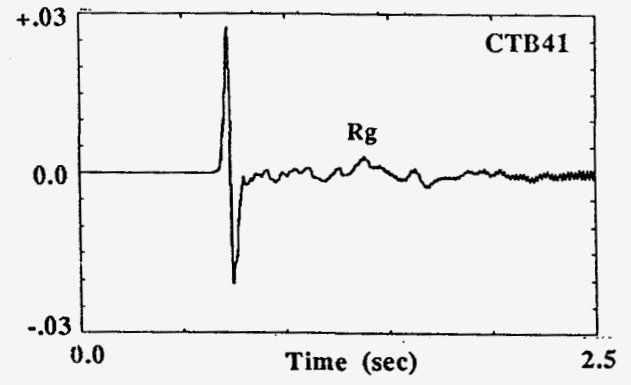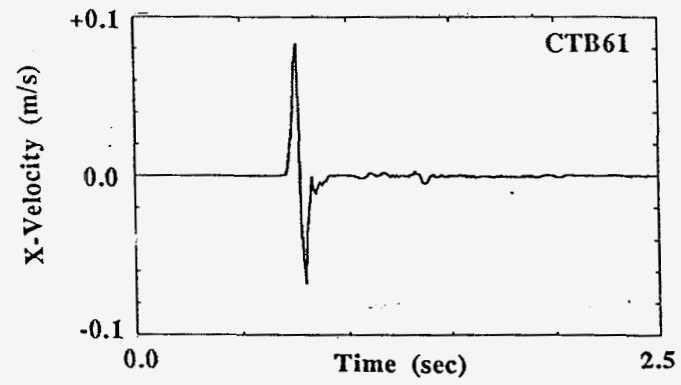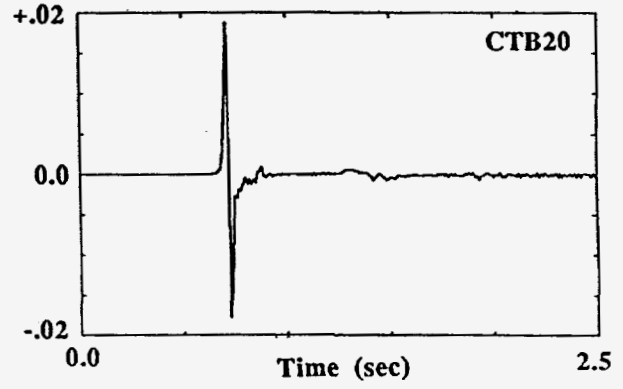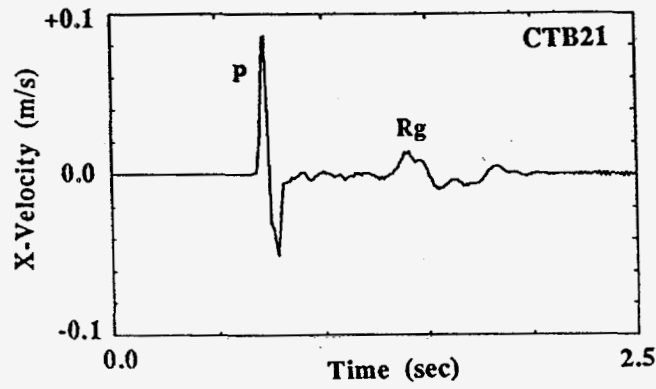
Fig. 4 Radial (x-component) particle velocity at 4320 m surface range for CTB21, CTB20, CTB61 and CTB41 calculations. Plot scaling adjusted to peak amplitudes. No filtering.
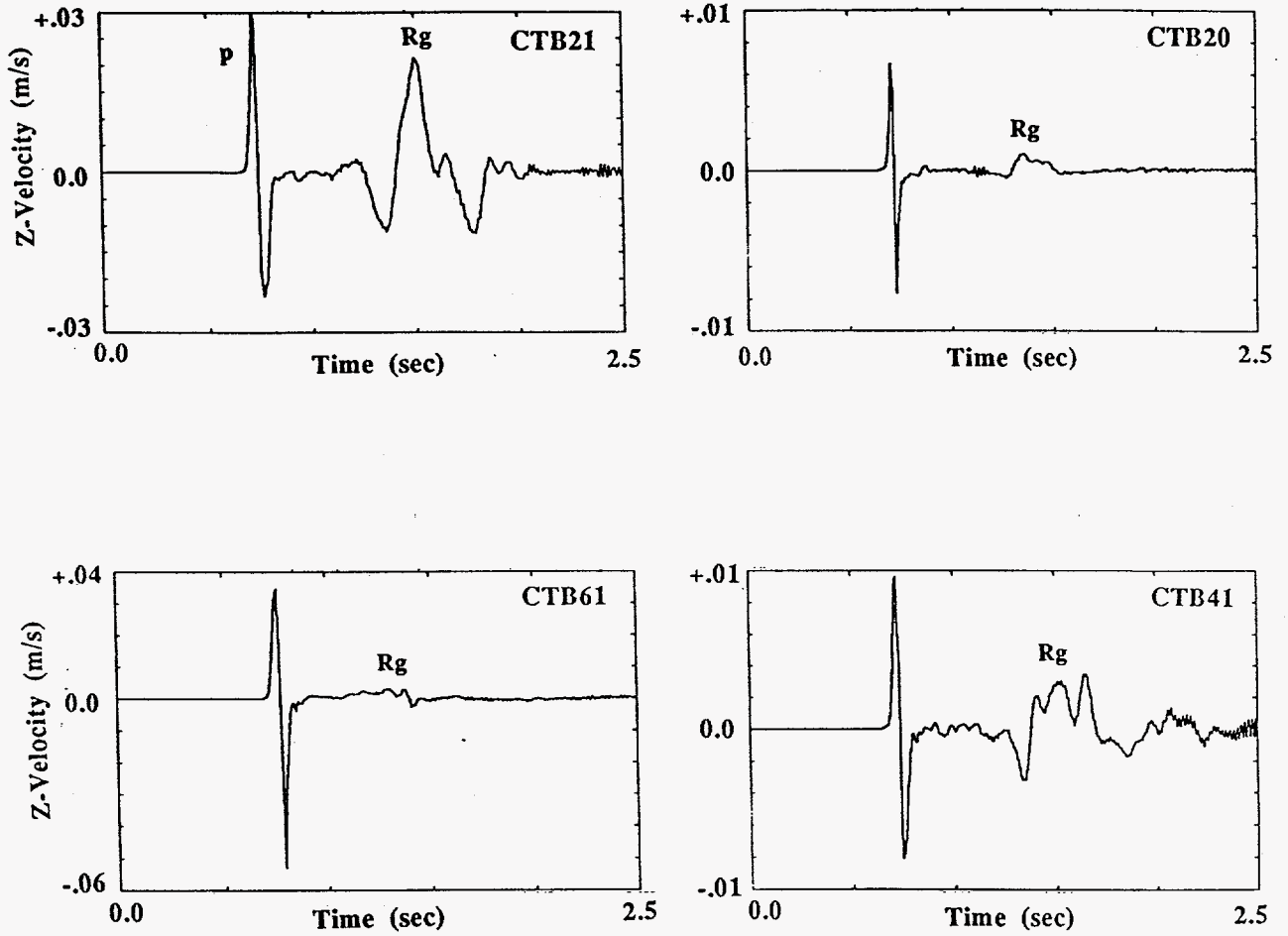
Fig. 5 Vertical (z-component) particle velocity at 4320 m surface range for CTB21, CTB20, CTB61, and CTB 41 calculations. Plot scaling adjusted to peak amplitudes. No filtering.
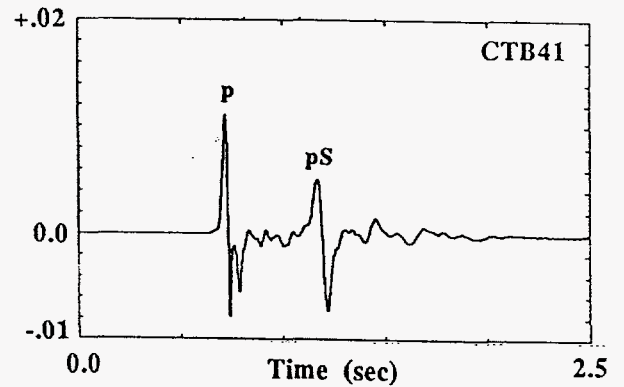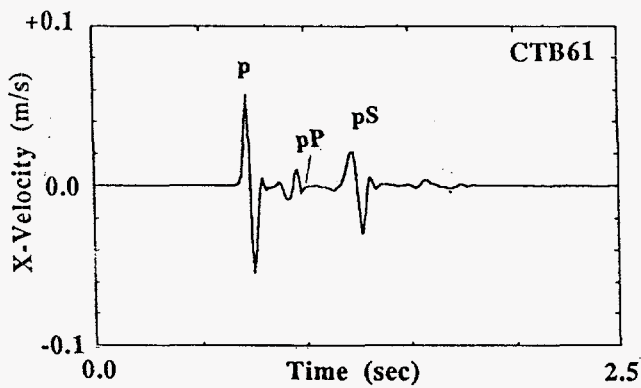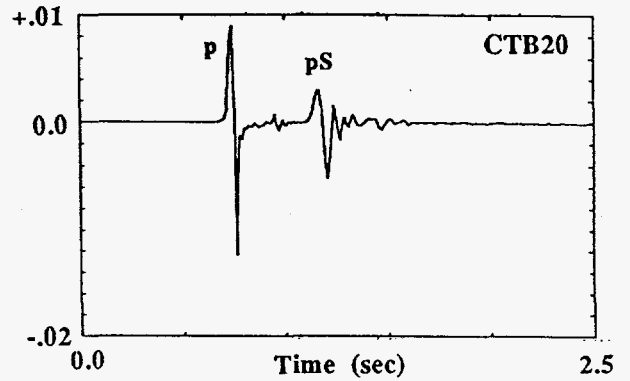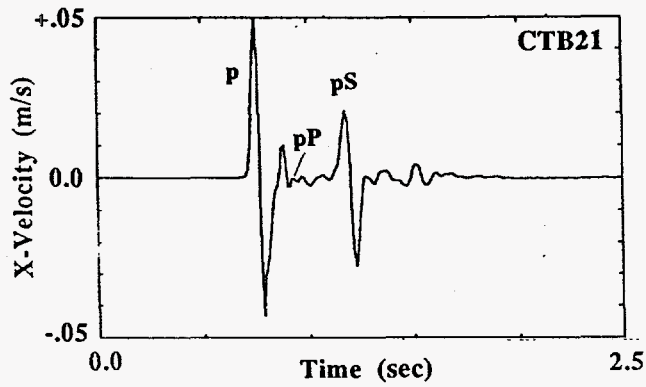
Fig. 6 Radial (x-component) particle velocity at 4320 m horizontal range, depth = 1920 m, for CTB21, CTB20, CTB61, and CTB41 calculations. Plot scaling adjusted to peak amplitudes. No filtering.
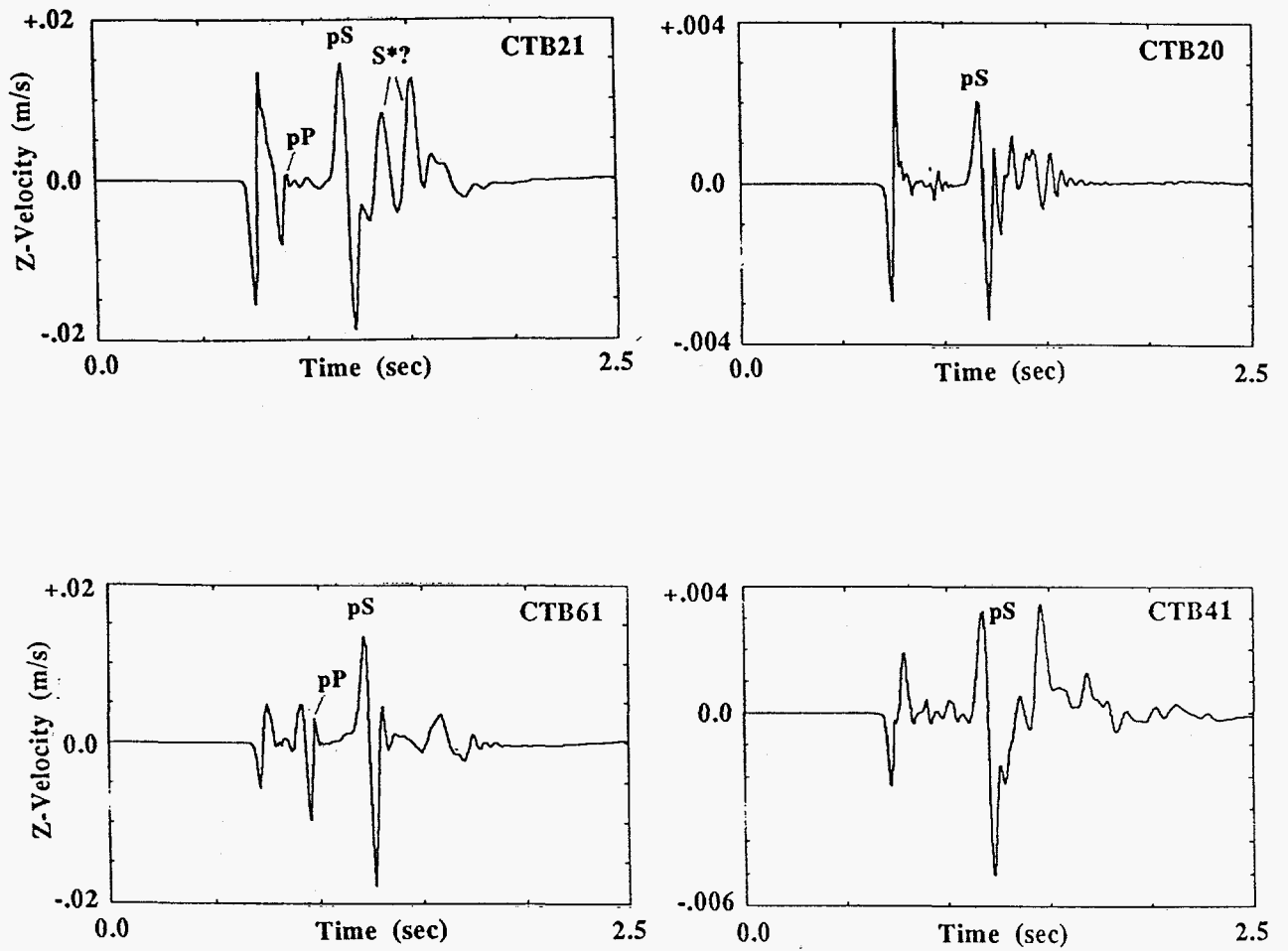
Fig. 7 Vertical (z-component) particle velocity at 4320 m horizontal range, depth = 1920 m, for CTB 21, CTB20, CTB61, and CTB41 calculations. Plot scaling adjusted to peak amplitudes. No filtering.

Page intentionally left blank
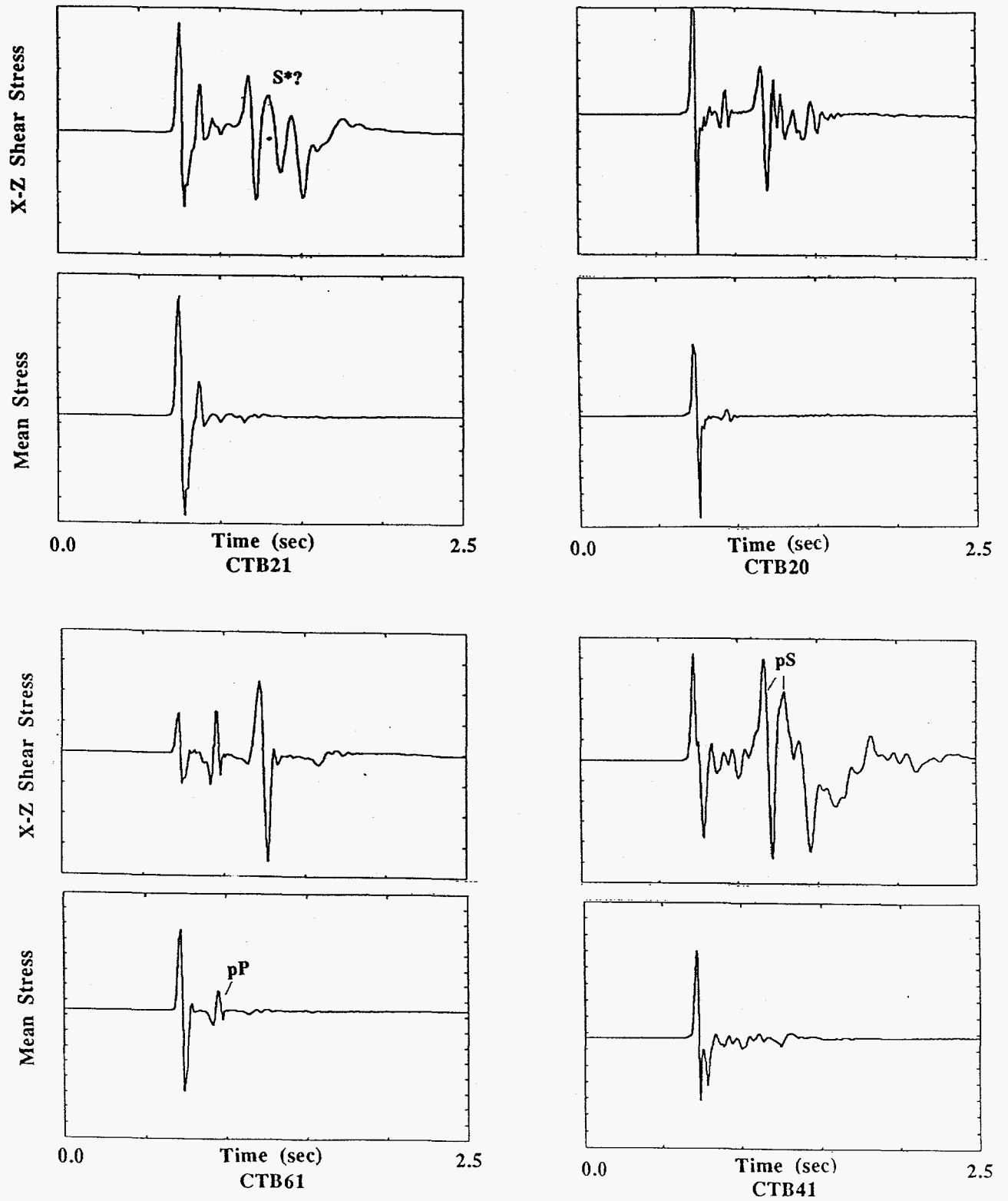
Fig. 8 Mean stress (pressure) and x-z shear stress time histories for CTB21, CTB20, CTB61, and CTB41 calculations at horizontal range = 4320 m, depth = 1920 m, z-component only. Amplitude scales not provided.

Surface

Depth (km)

S*?

pS

pP

p-wave

2.4

1.0 Horizontal Range (km) **5.0**

CTB21

Surface

Depth (km)

S*?

pS

false reflection

pP

p-wave

2.4

1.0 Horizontal Range (km) **5.0**
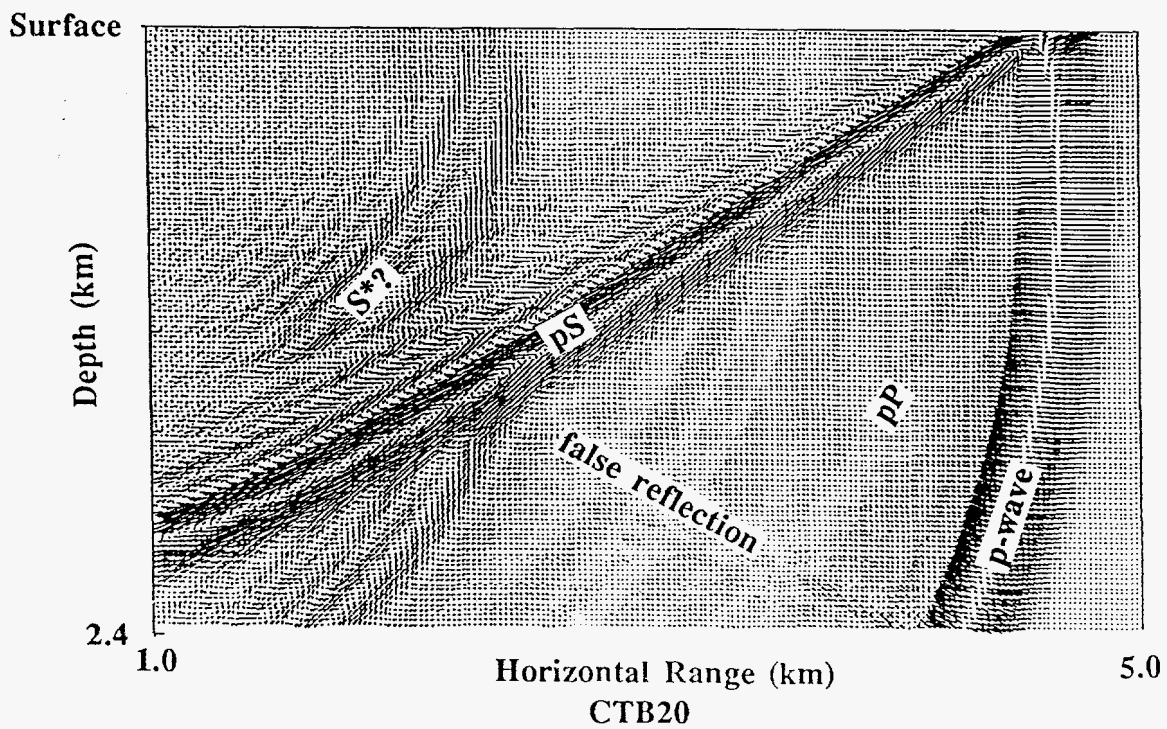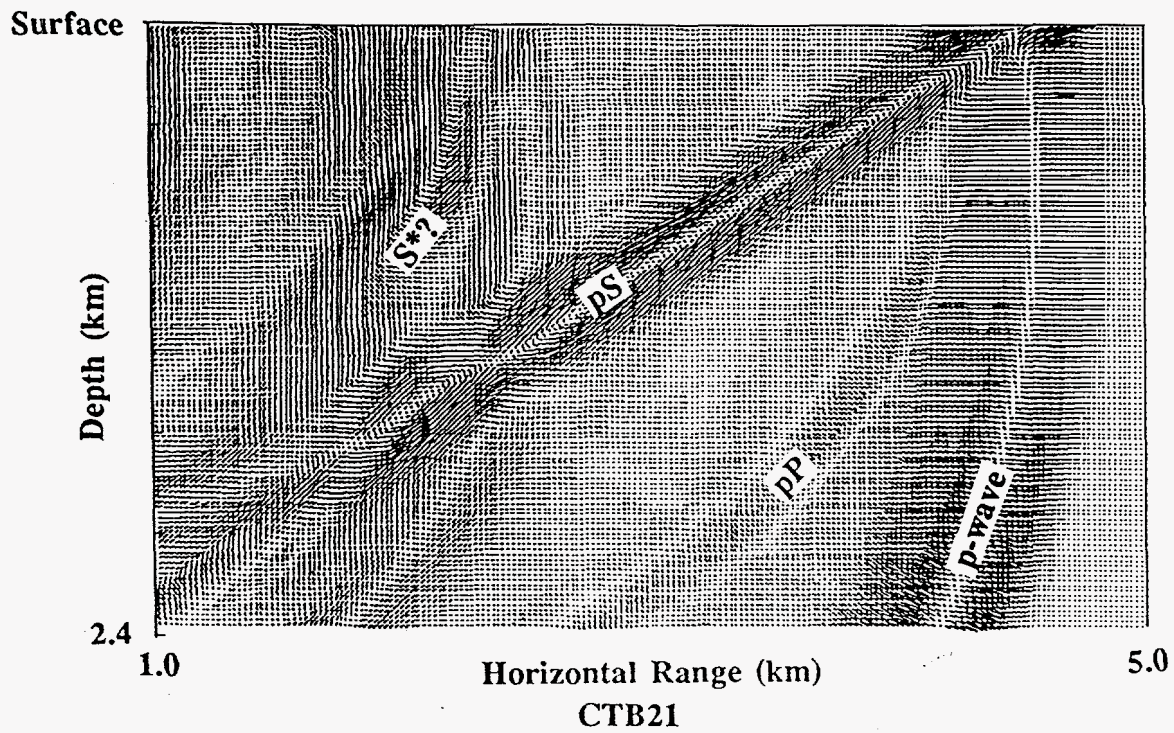
CTB20

Fig. 9 Particle velocity field at 740 ms for CTB21 (upper) and CTB20 (lower). Vector lengths are proportional to amplitude and directions indicate direction of flow.
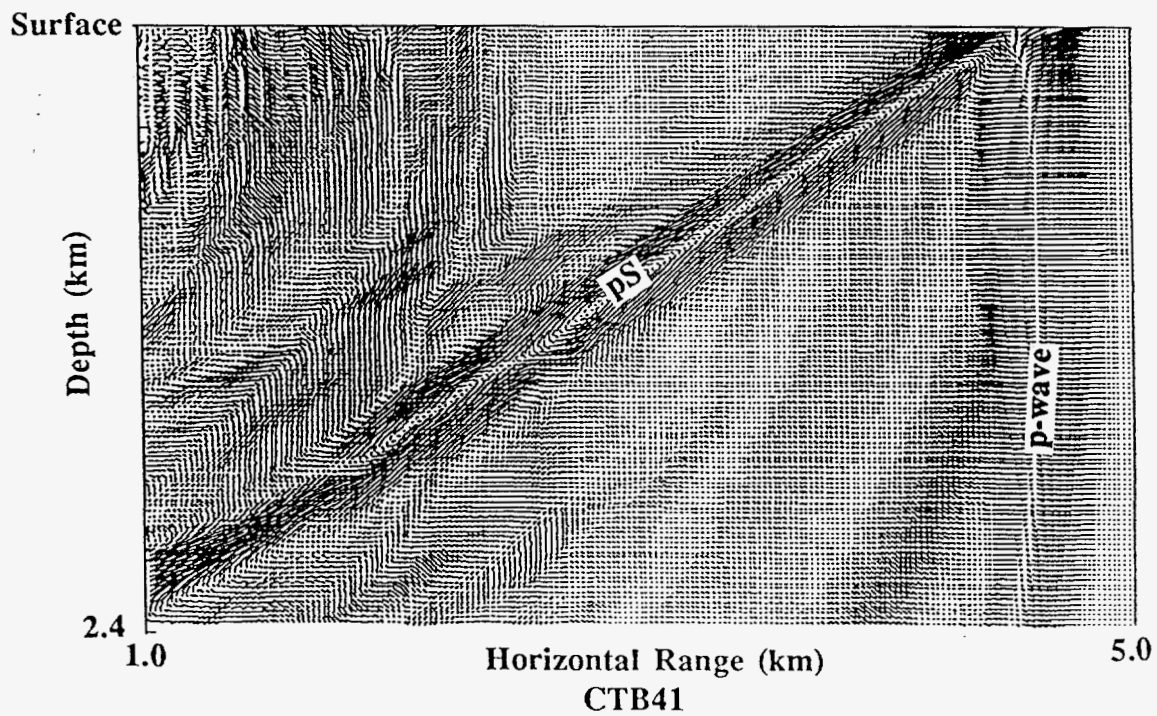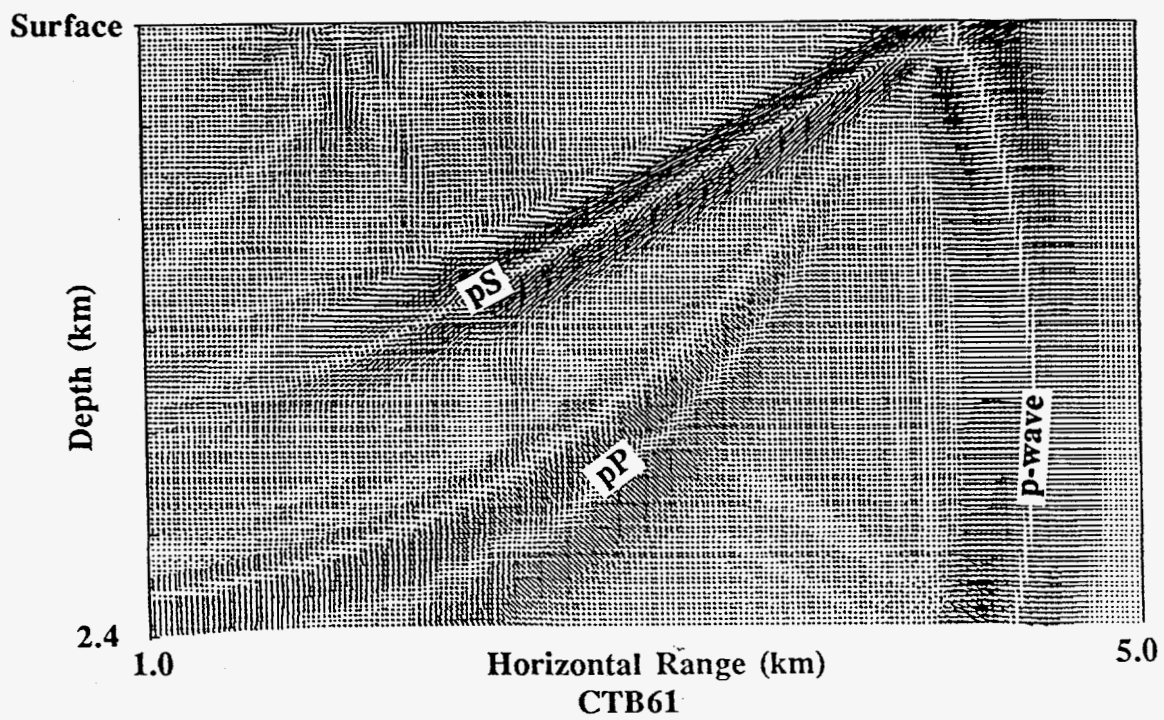
Fig. 10 Particle velocity field at 740 ms for CTB61 (upper) and CTB41 (lower). Vector lengths are proportional to amplitude and directions indicate direction of flow.
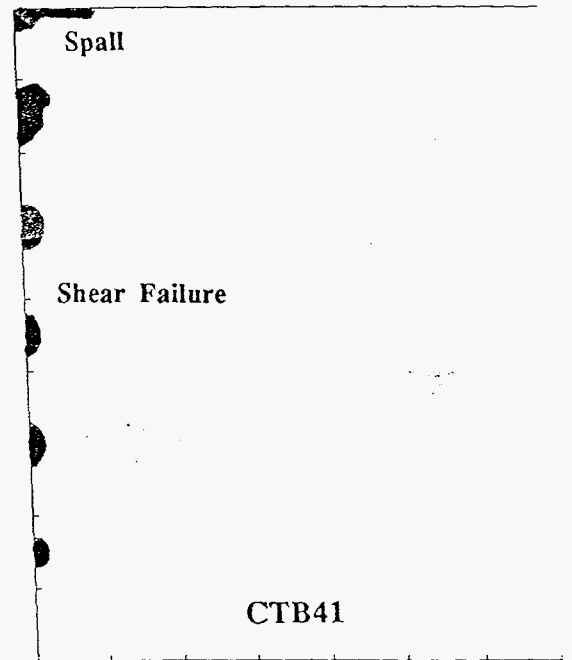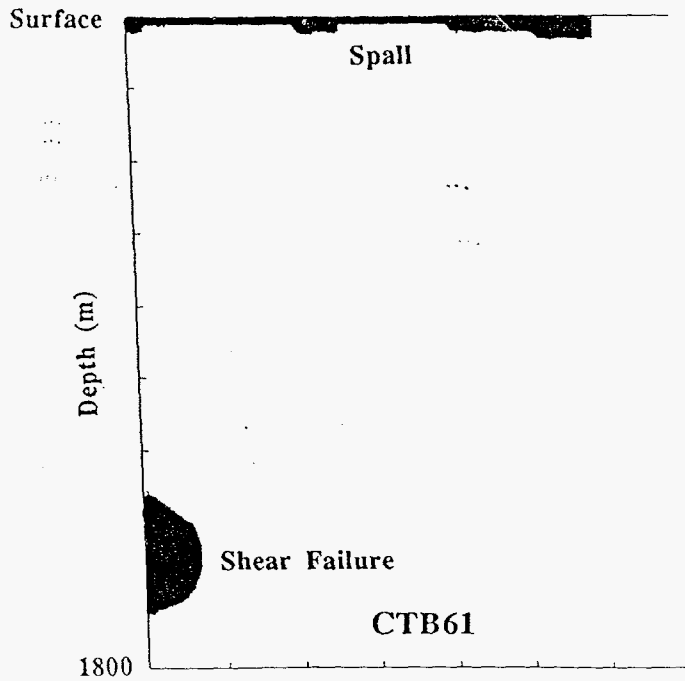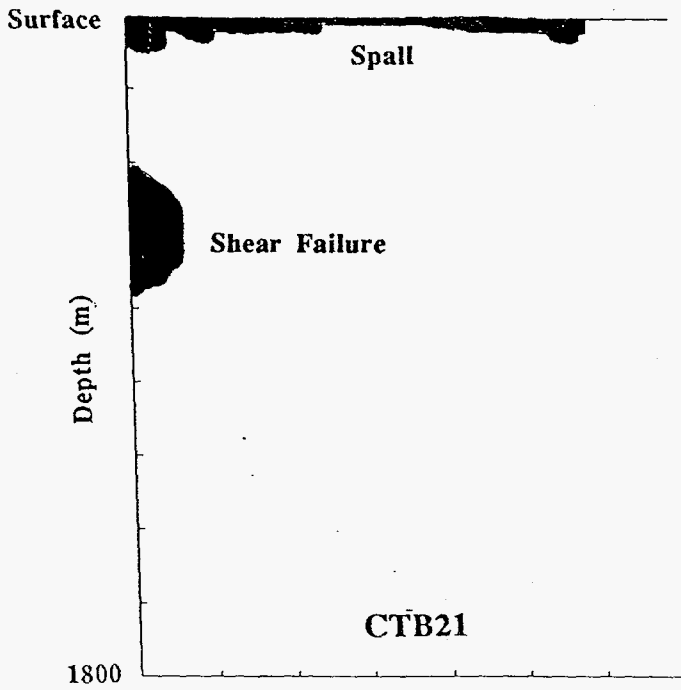
Fig. 11 Regions of material shear failure and spall for CTB21, CTB61, and CTB41–indicated as blackened areas. Shear failure region shown is maximum extent of failure; spalled region is at time of maximum horizontal extent of spall, not necessarily maximum depth. The vertical and horizontal scales are the same.
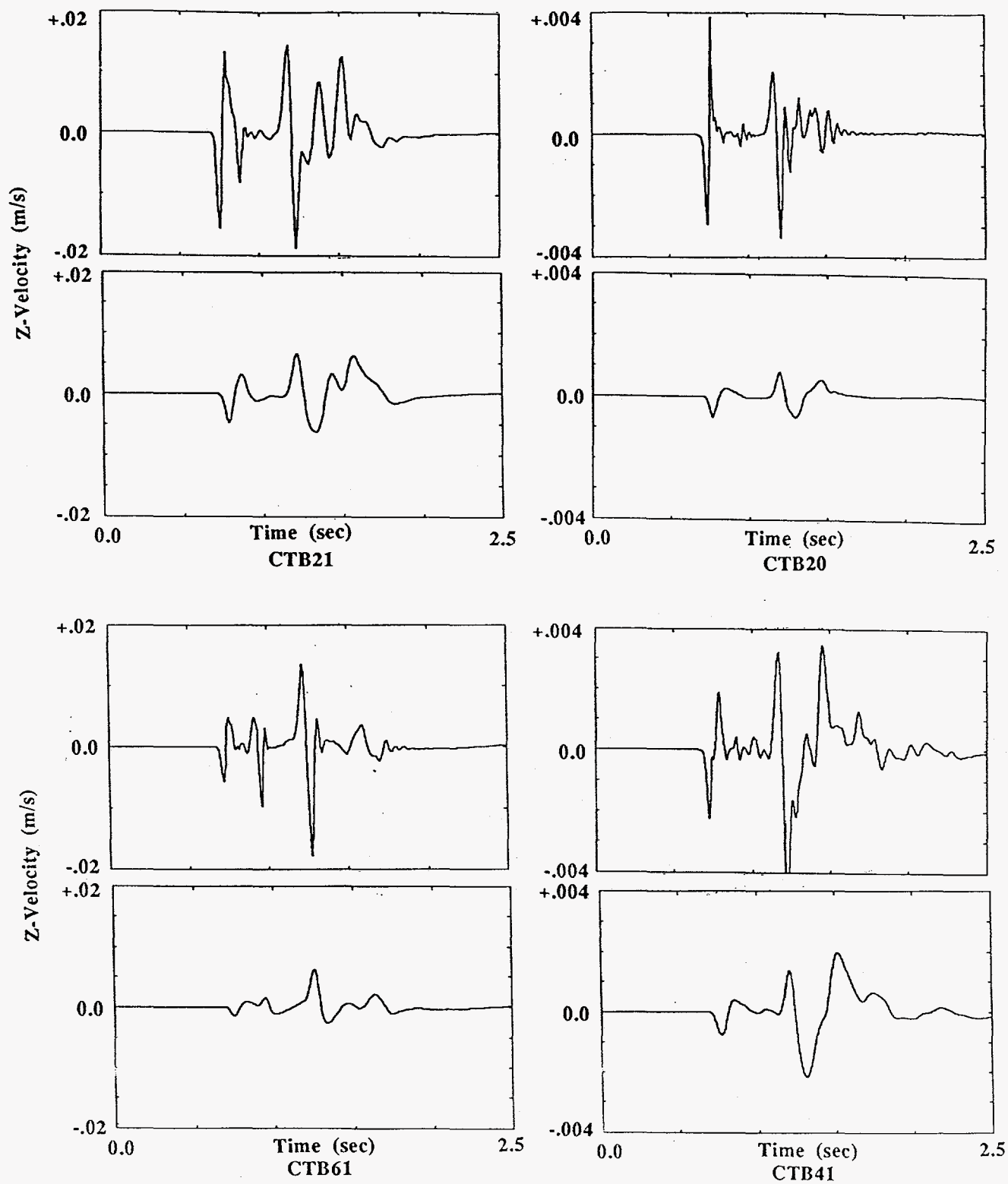
Fig. 12 Comparison of unfiltered and 4 Hz low pass filtered waveforms for CTB21, CTB20, CTB61, and CTB41 calculations at horizontal range = 4320 m, depth = 1920 m. Each filtered-unfiltered pair has the same amplitude scaling but scaling varies from case to case.
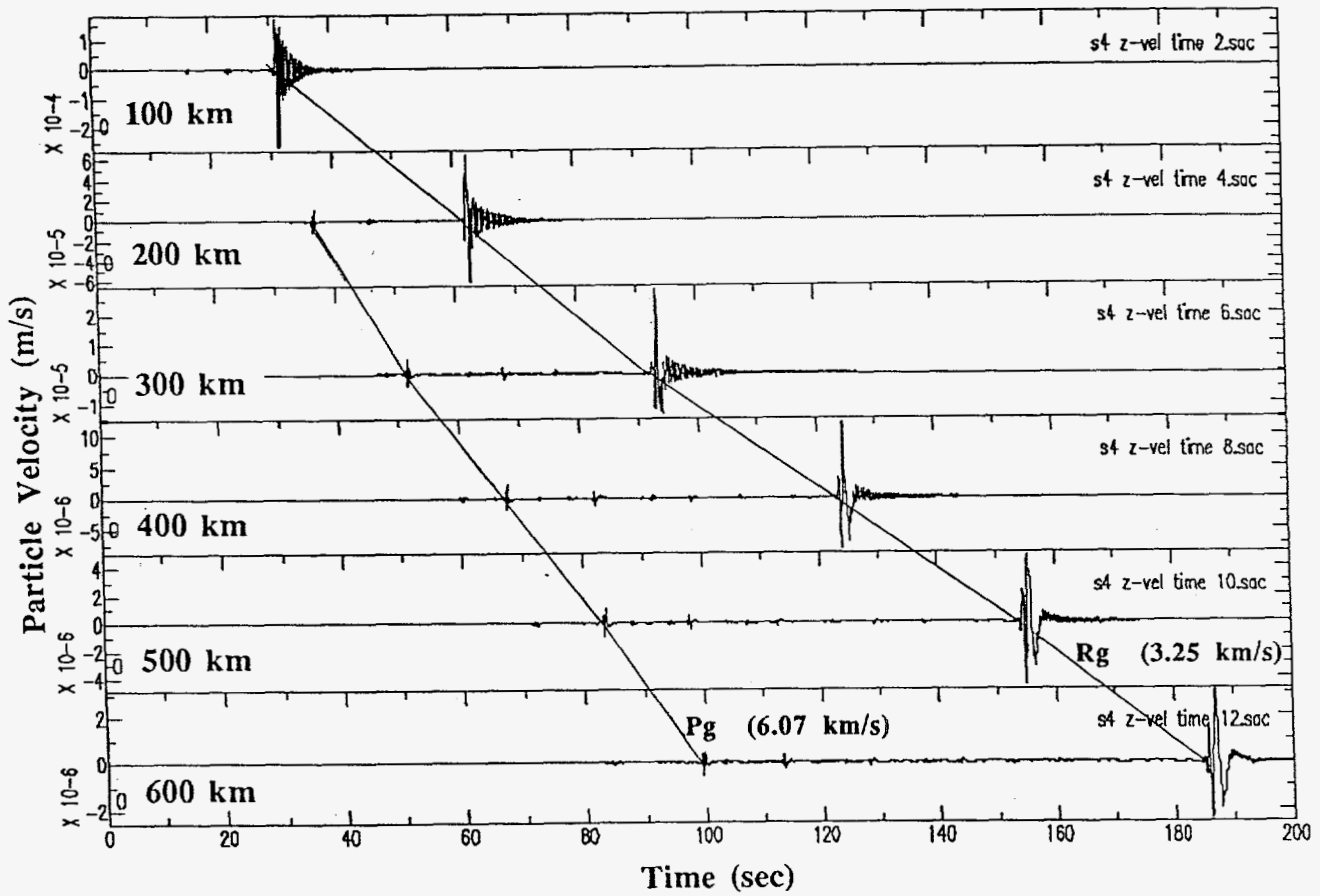
Fig. 13 Evolution of the seismic signal along the surface from 100 to 600 km range for CTB21 calculation. Vertical component with scaling at each distance adjusted to peak amplitude. Lines connecting specific phases are not straight because of unequal spacing between traces. Velocities are averaged values to 600 km distance.
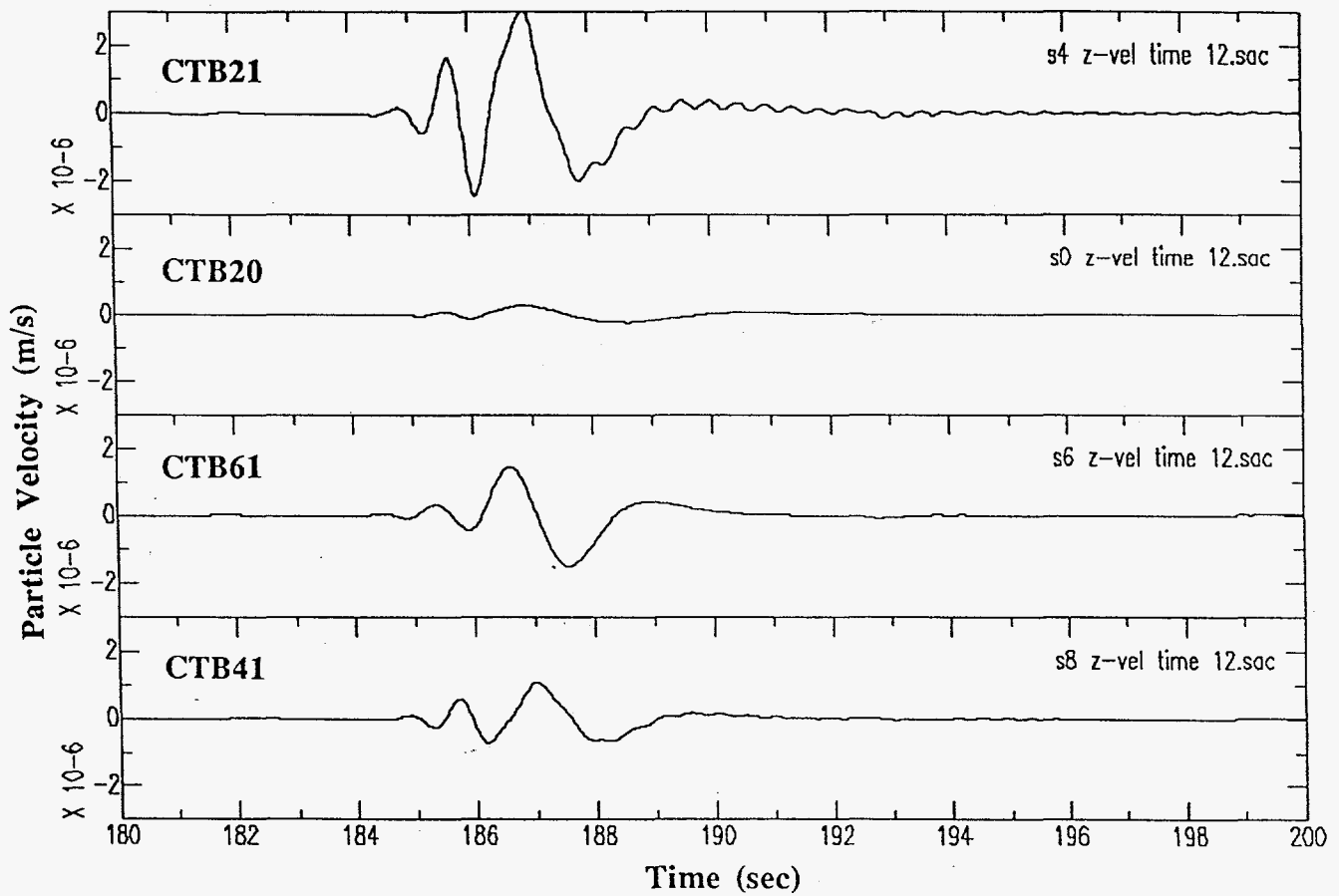
Fig. 14 Comparison of Rg phases (180 to 200 sec) at 600 km for CTB21, CTB20, CTB61, and CTB41 calculations. Vertical component. Fixed amplitude scaling to the velocity range -2×10^{-6} to 3×10^{-6} m/s.
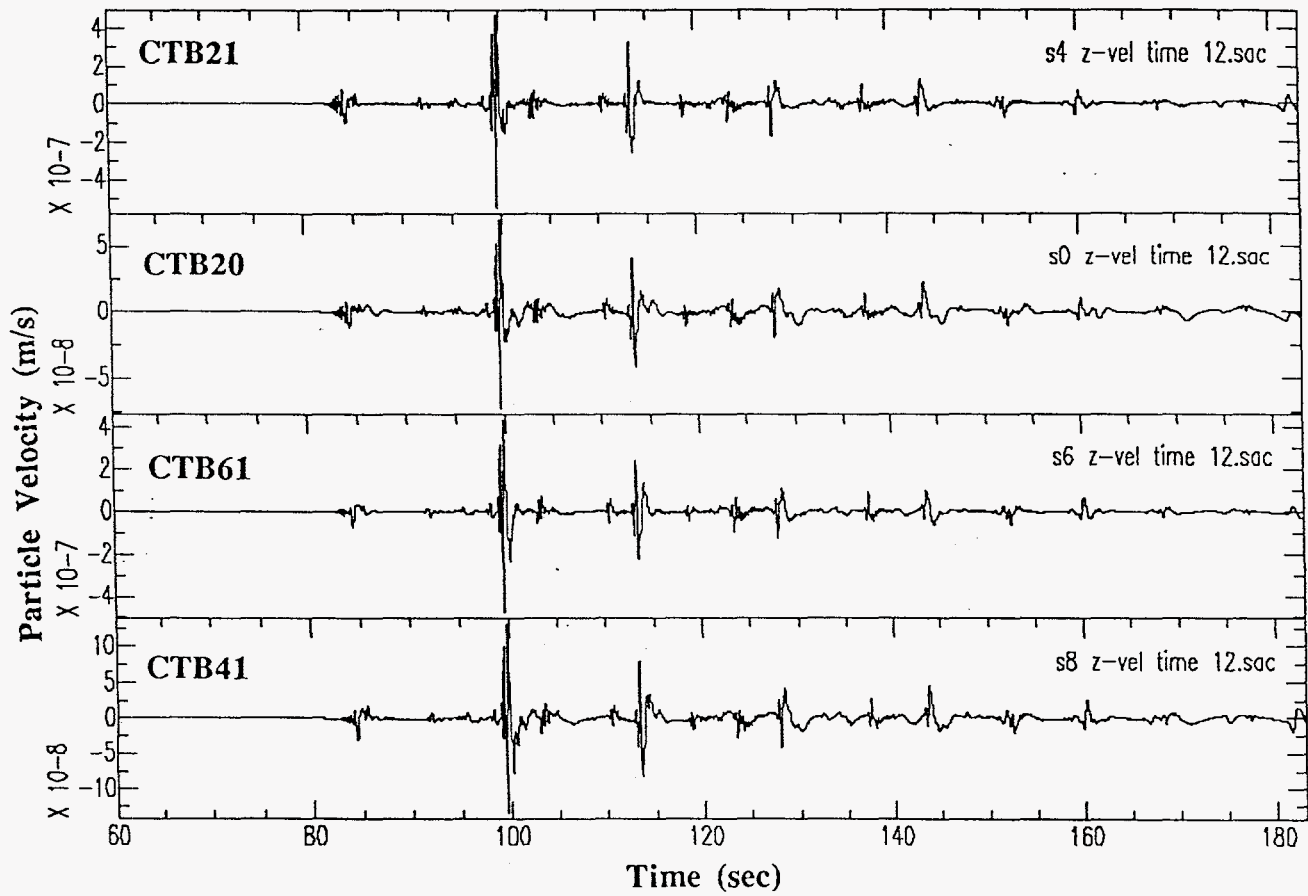
Fig. 15 Comparison of pre-Rg phases (60 to 183 sec) at 600 km for CTB21, CTB20, CTB61, and CTB41 calculations. Vertical component. Plot scaling to peak amplitude.
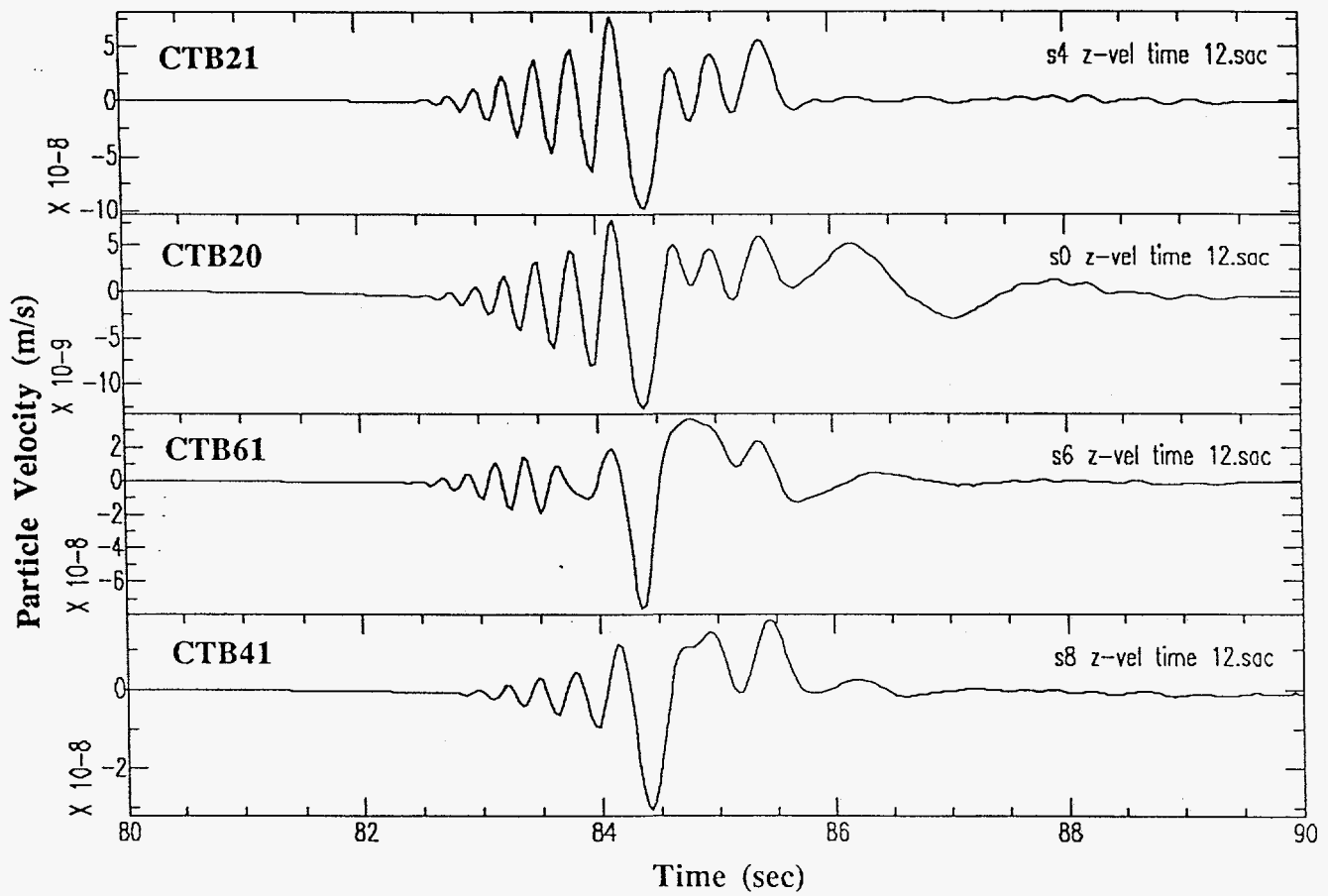
Fig. 16 Comparison of P-wave arrivals (80 to 90 sec) at 600 km for CTB21, CTB20, CTB61, and CTB41 calculations. Vertical component. Plot scaling to peak amplitude.
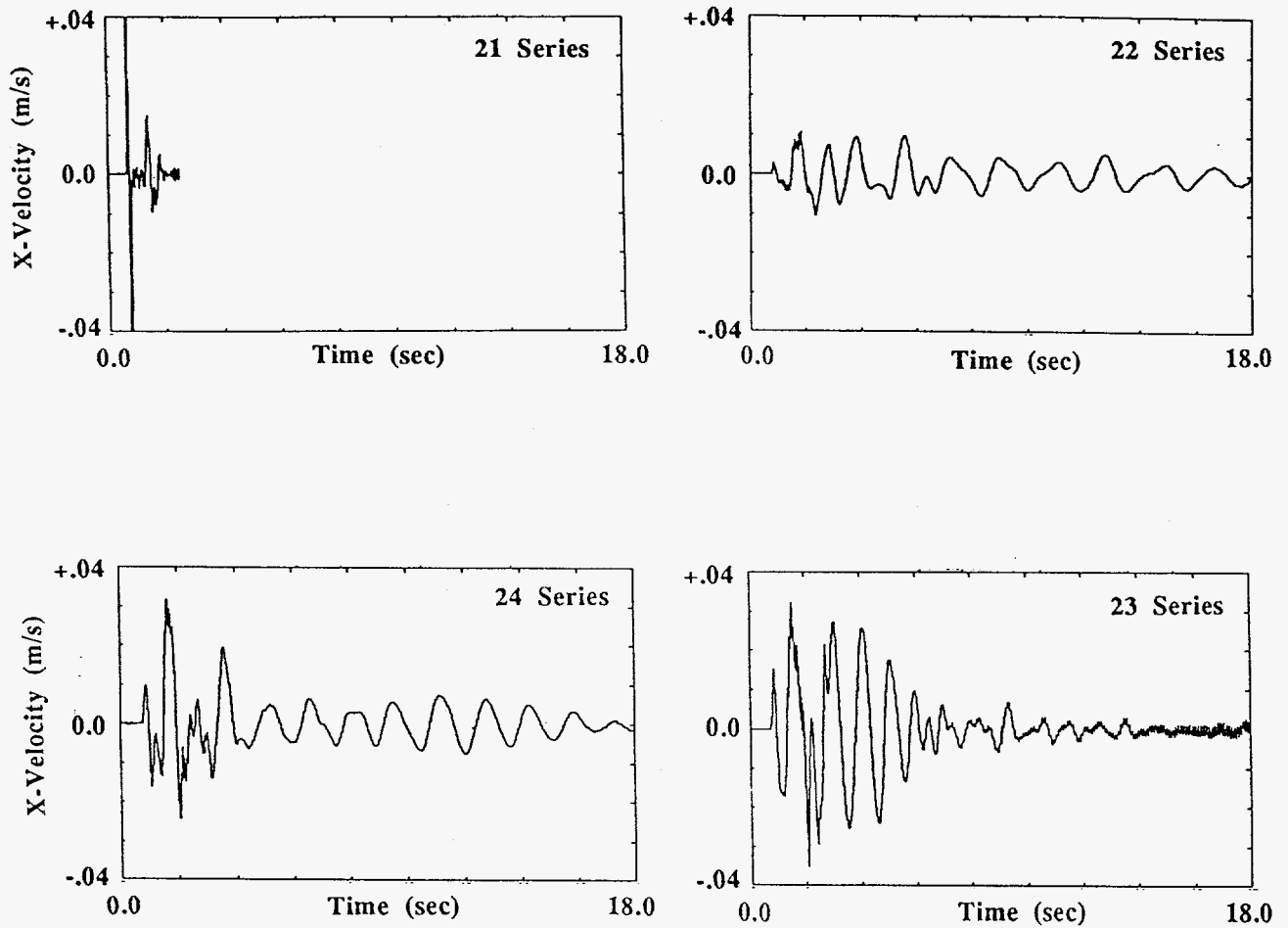
Fig. 17   Radial (x-component) particle velocity at 4320 m surface range for 21, 22, 23, and 24 series calculations. Fixed amplitude scaling to velocity range -.04 to .04 m/s.   No filtering.
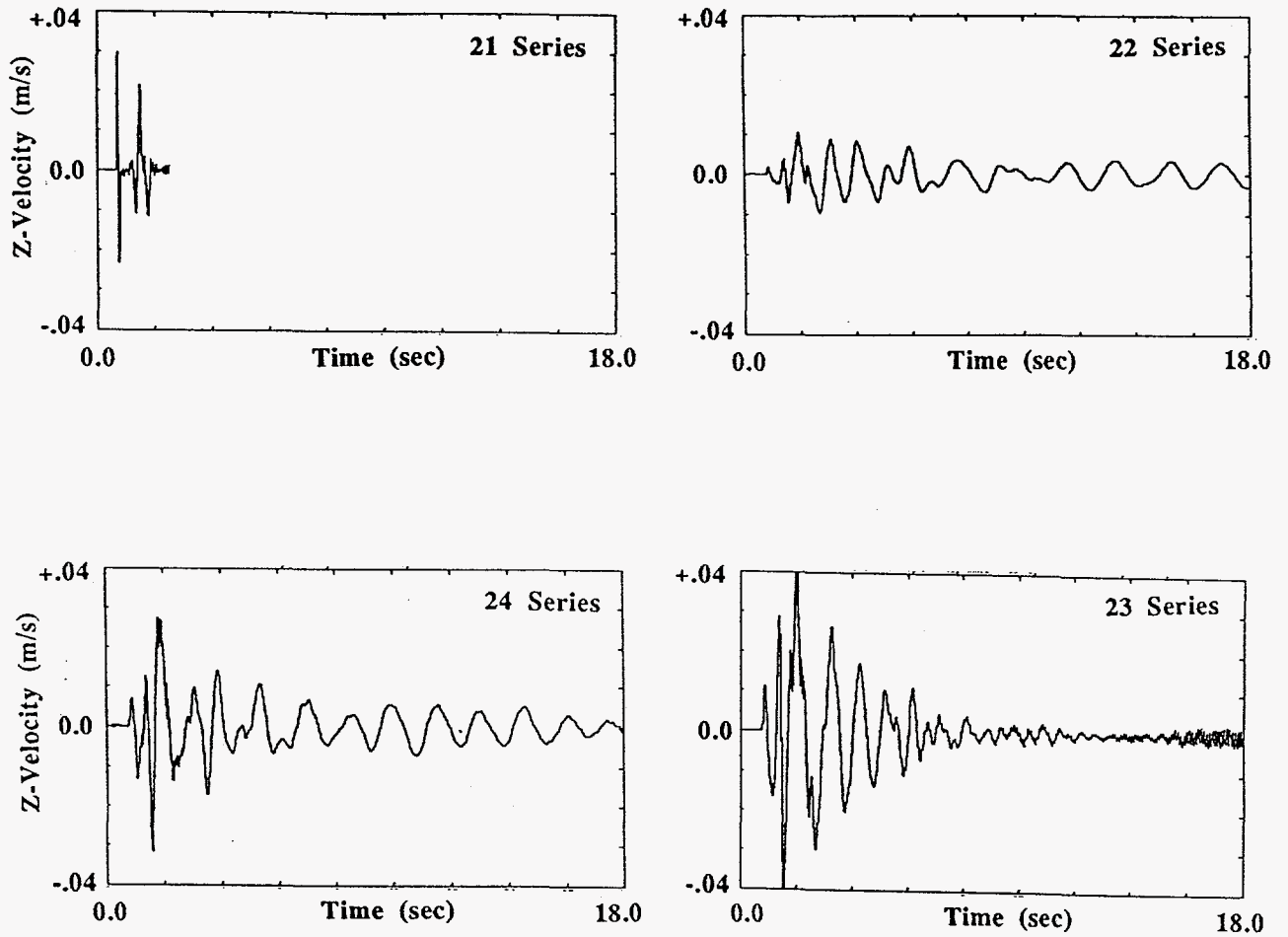
Fig. 18 Vertical (z-component) particle velocity at 4320 m surface range for 21, 22, 23, and 24 series calculations. Fixed amplitude scaling to velocity range -.04 to .04 m/s. No filtering.
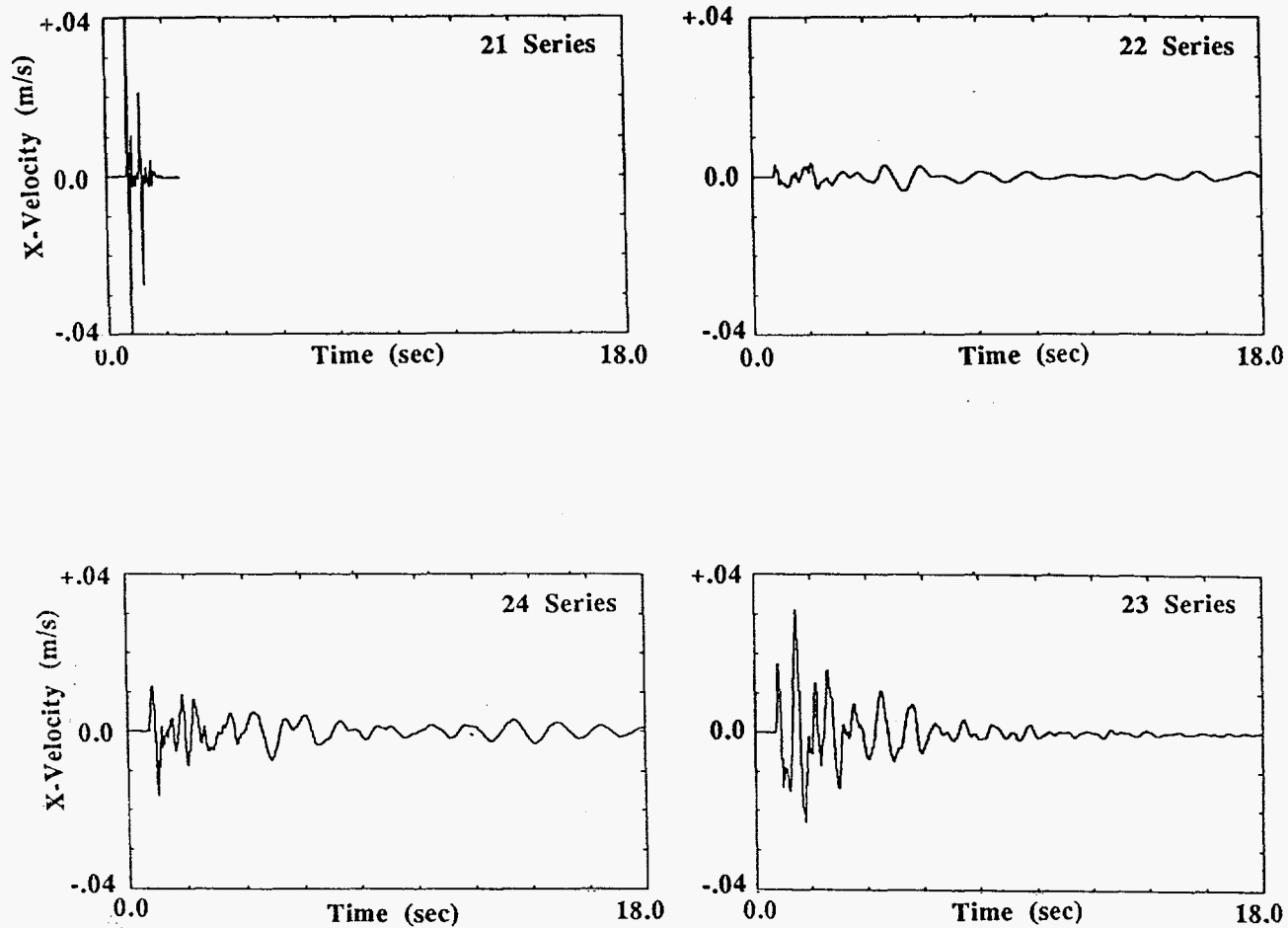
Fig. 19 Radial (x-component) particle velocity at 4320 m horizontal range, depth = 1920 m, for 21, 22, 23, and 24 series calculations. Fixed amplitude scaling to velocity range -.04 to .04 m/s. No filtering.
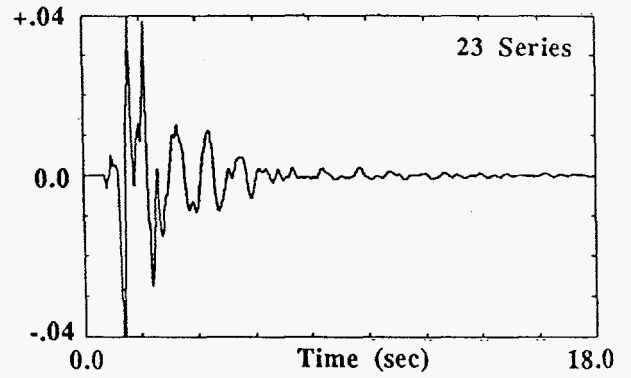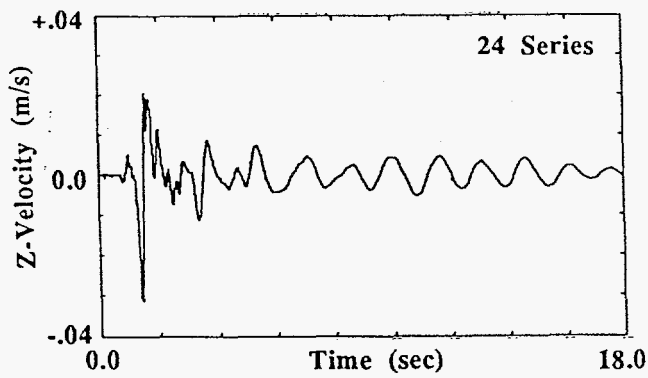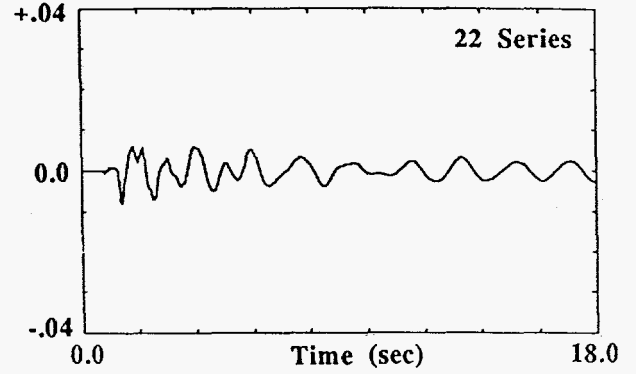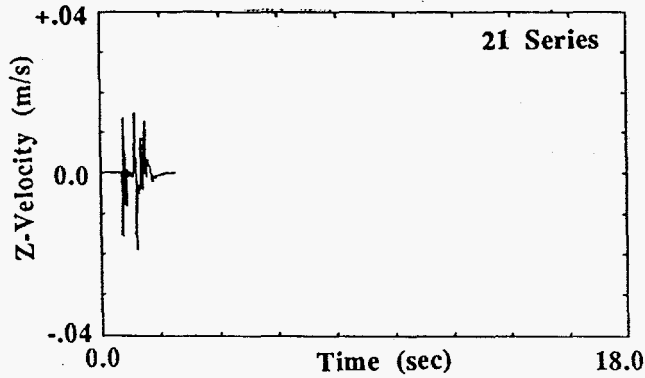
Fig. 20 Vertical (z-component) particle velocity at 4320 m horizontal range, depth = 1920 m, for 21, 22, 23, and 24 series calculations. Fixed amplitude scaling to velocity range -.04 to .04 m/s. No filtering.

Page intentionally left blank
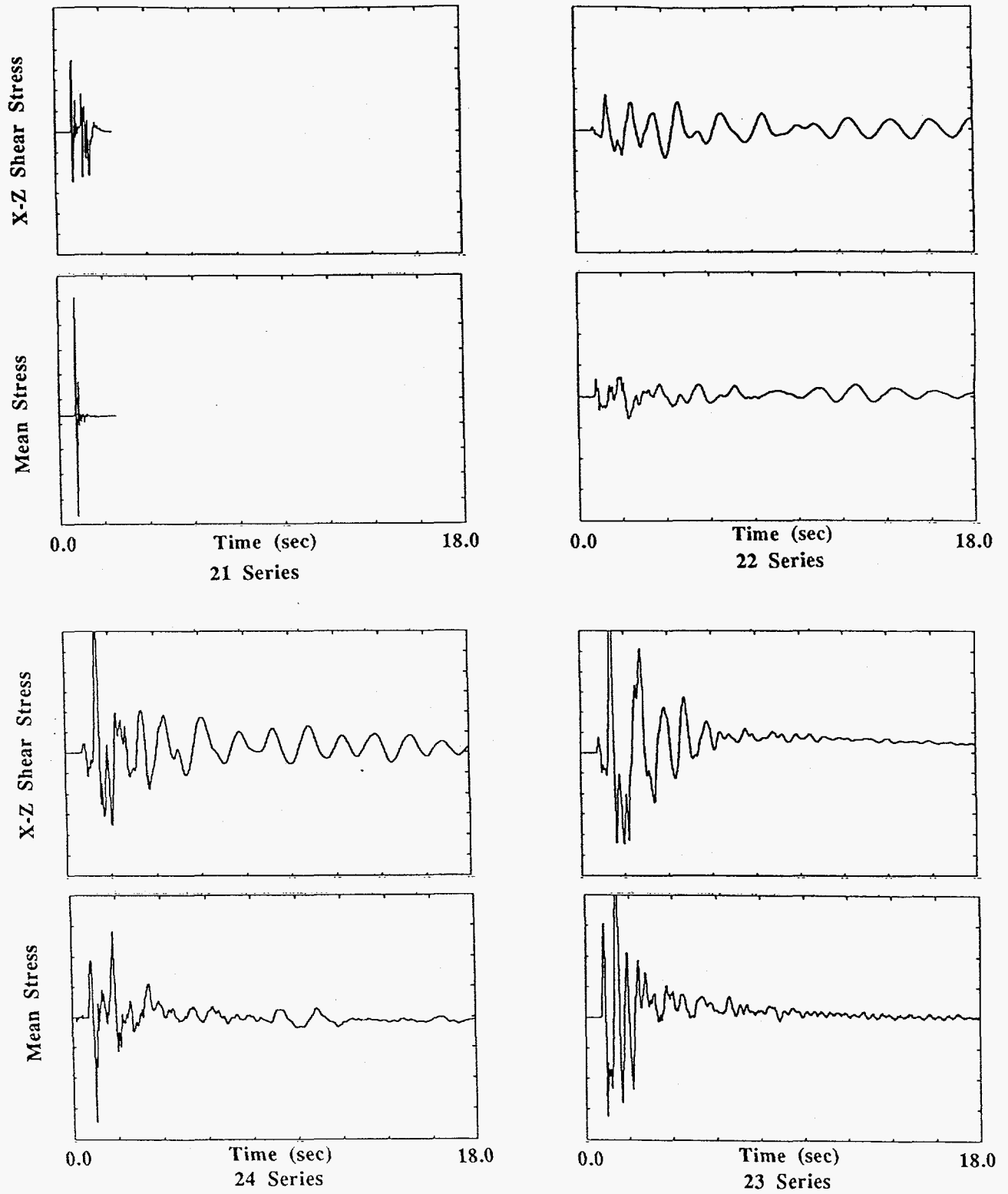
Fig. 21 Mean stress (pressure) and x-z shear stress time histories for 21, 22, 23, and 24 series calculations at horizontal range = 4320 m, depth = 1920 m, z-component only. Amplitude scales not provided.
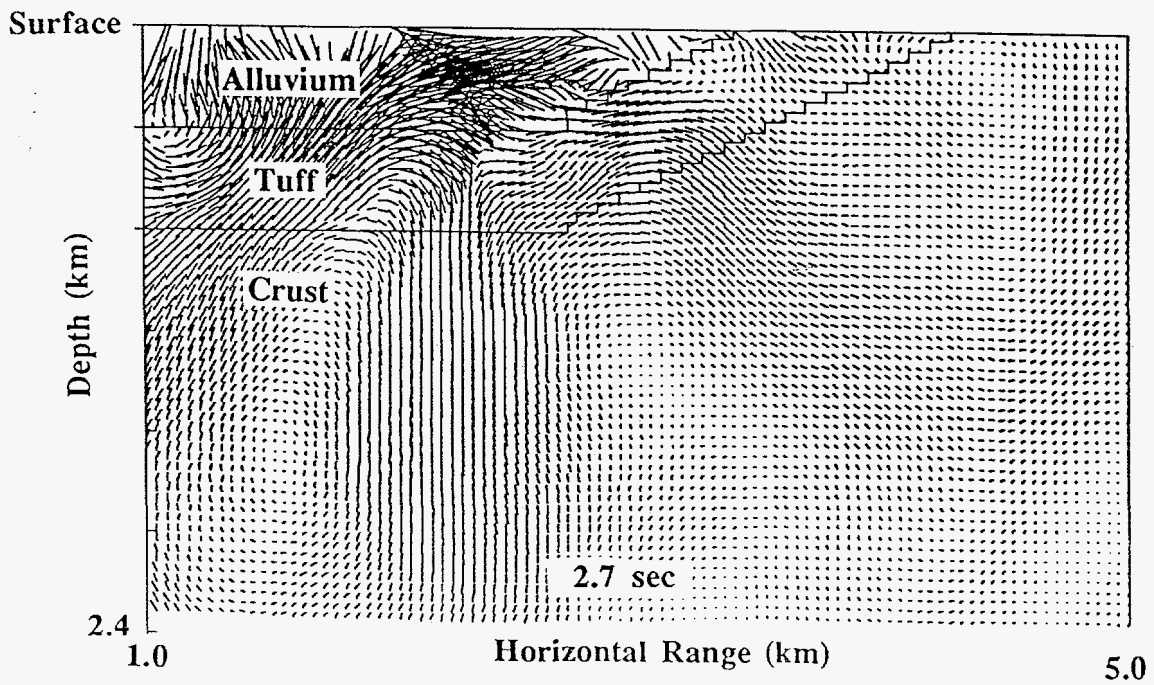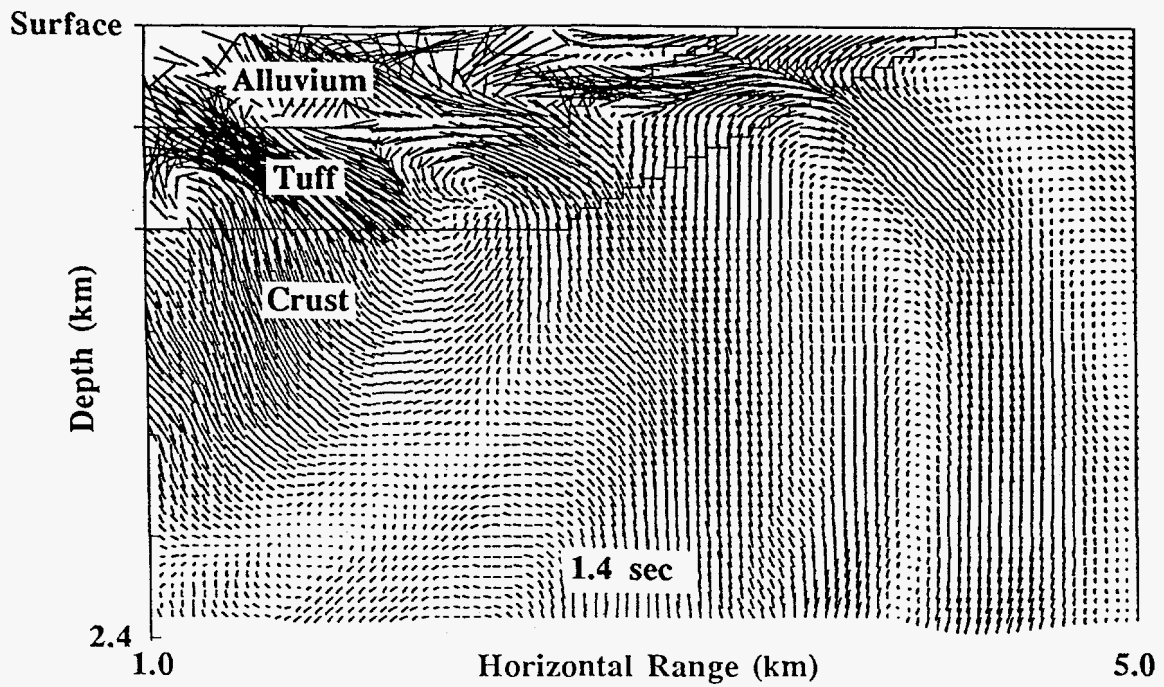
Fig. 22 Particle velocity field at 1.4 sec (upper) and 2.7 sec (lower) for 24 series calculations. Vector lengths are proportional to amplitude and directions indicate direction of flow.
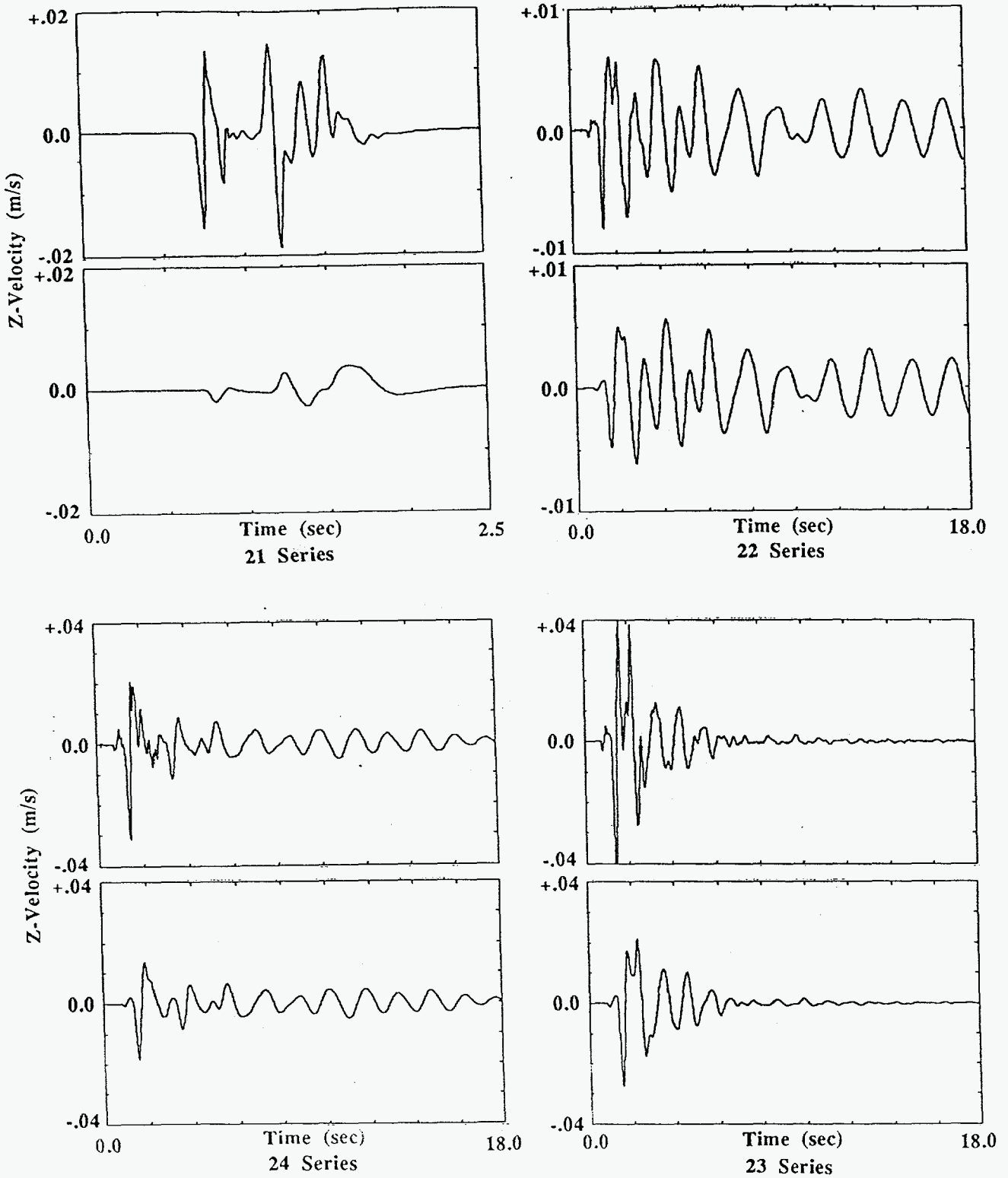
Fig. 23 Comparison of unfiltered and low pass filtered waveforms for 21, 22, 23, and 24 series calculations (21 is filtered at 2 Hz, the rest at 1.5 Hz) at horizontal range = 4320 m, depth = 1920 m. Each filtered-unfiltered pair has the same amplitude scaling but scaling varies from case to case.
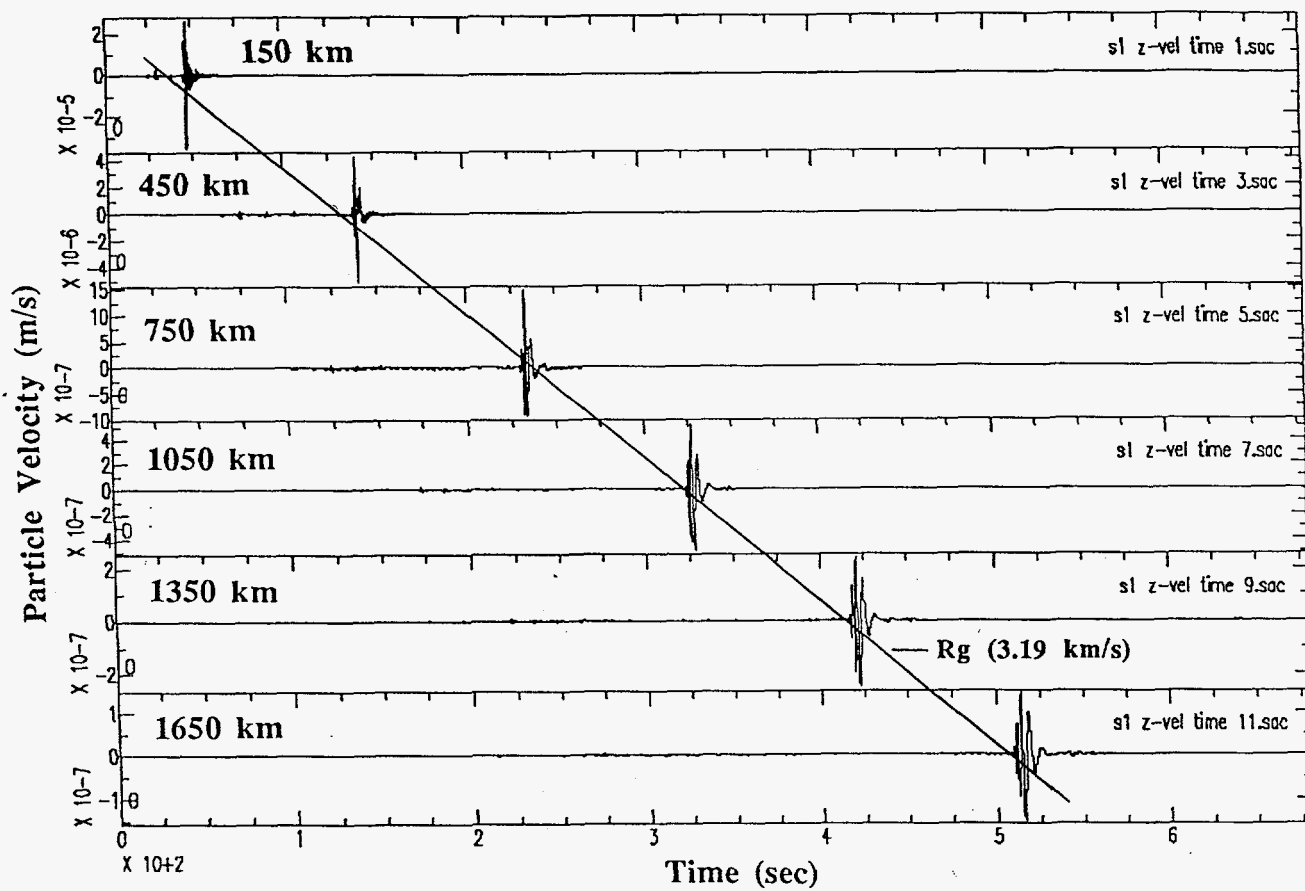
Fig. 24 Evolution of the seismic signal along the surface from 150 to 1650 km range for SCM21 calculation. Vertical component with scaling at each distance adjusted to peak amplitude.
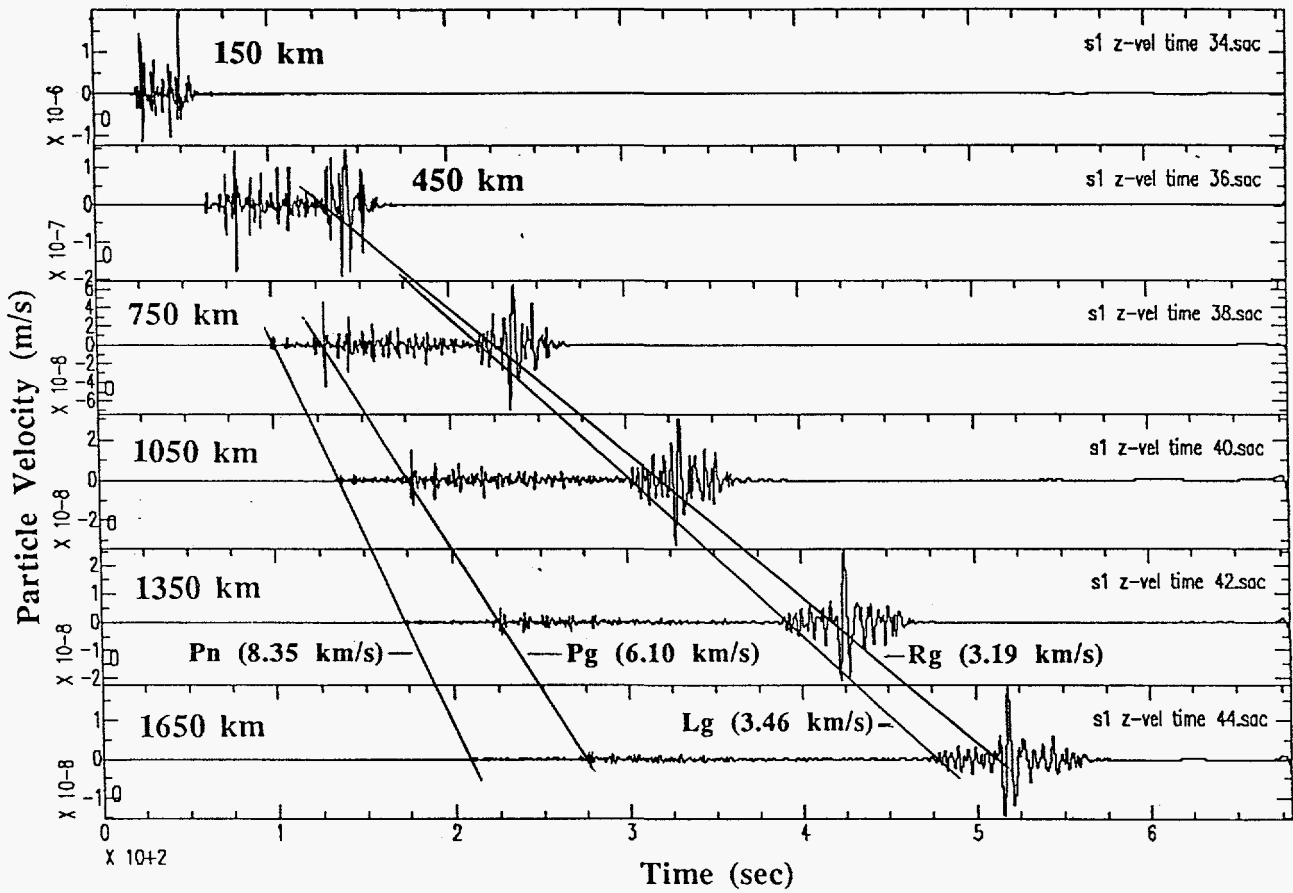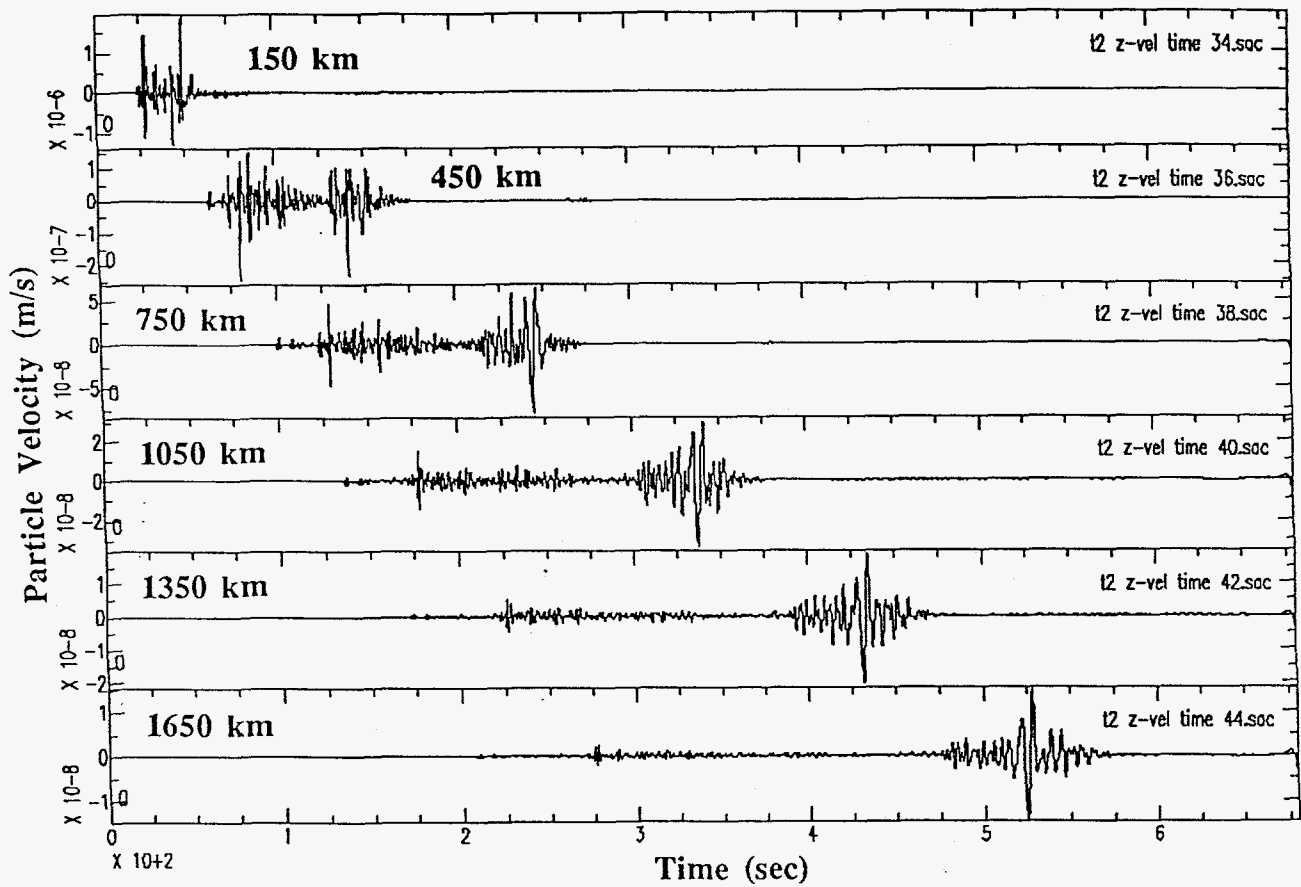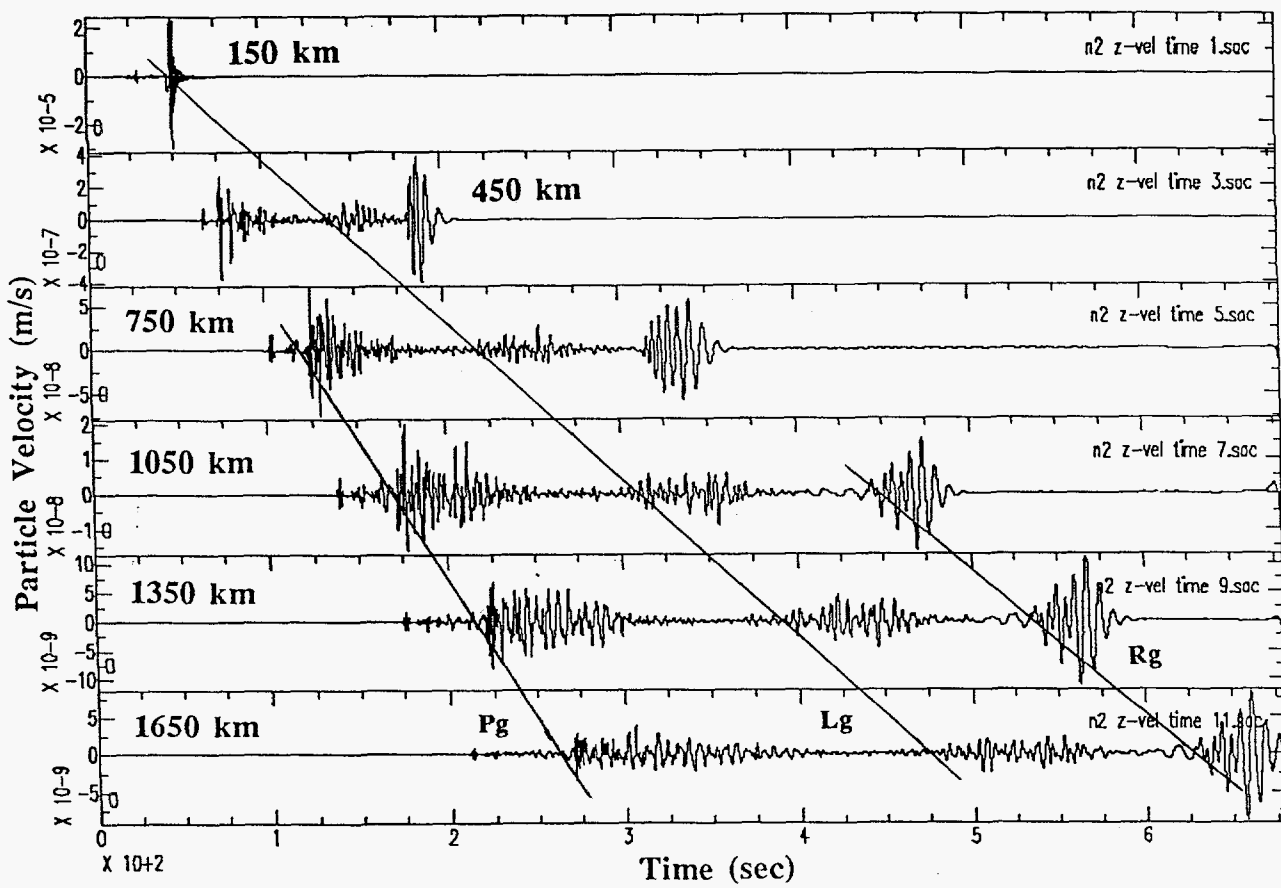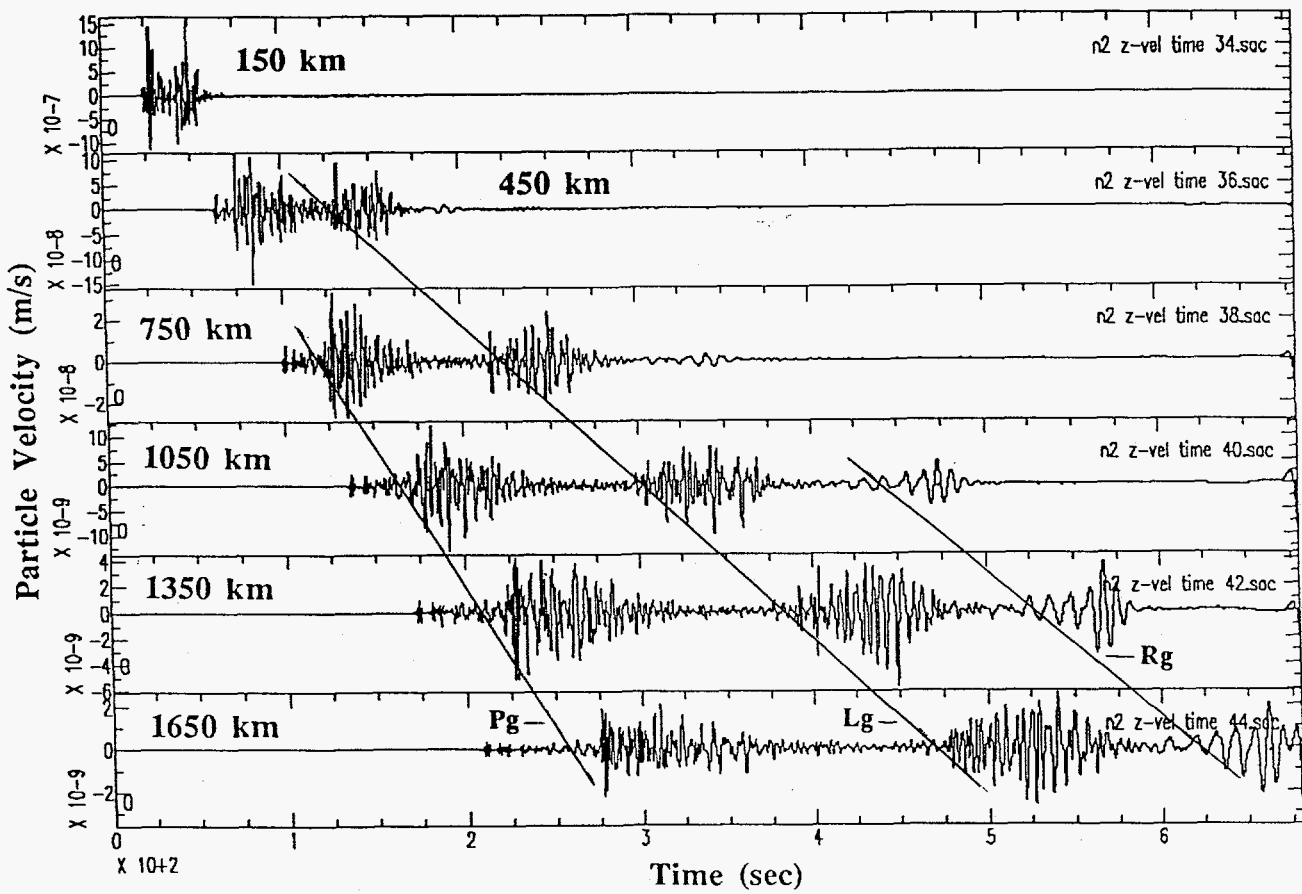
Fig. 25 Evolution of the seismic signal at 20 km depth from 150 to 1650 km horizontal range for SCM21 calculation. Vertical component with scaling at each distance adjusted to peak amplitude. The line for Rg represents the same velocity shown for Rg in Figure 24.
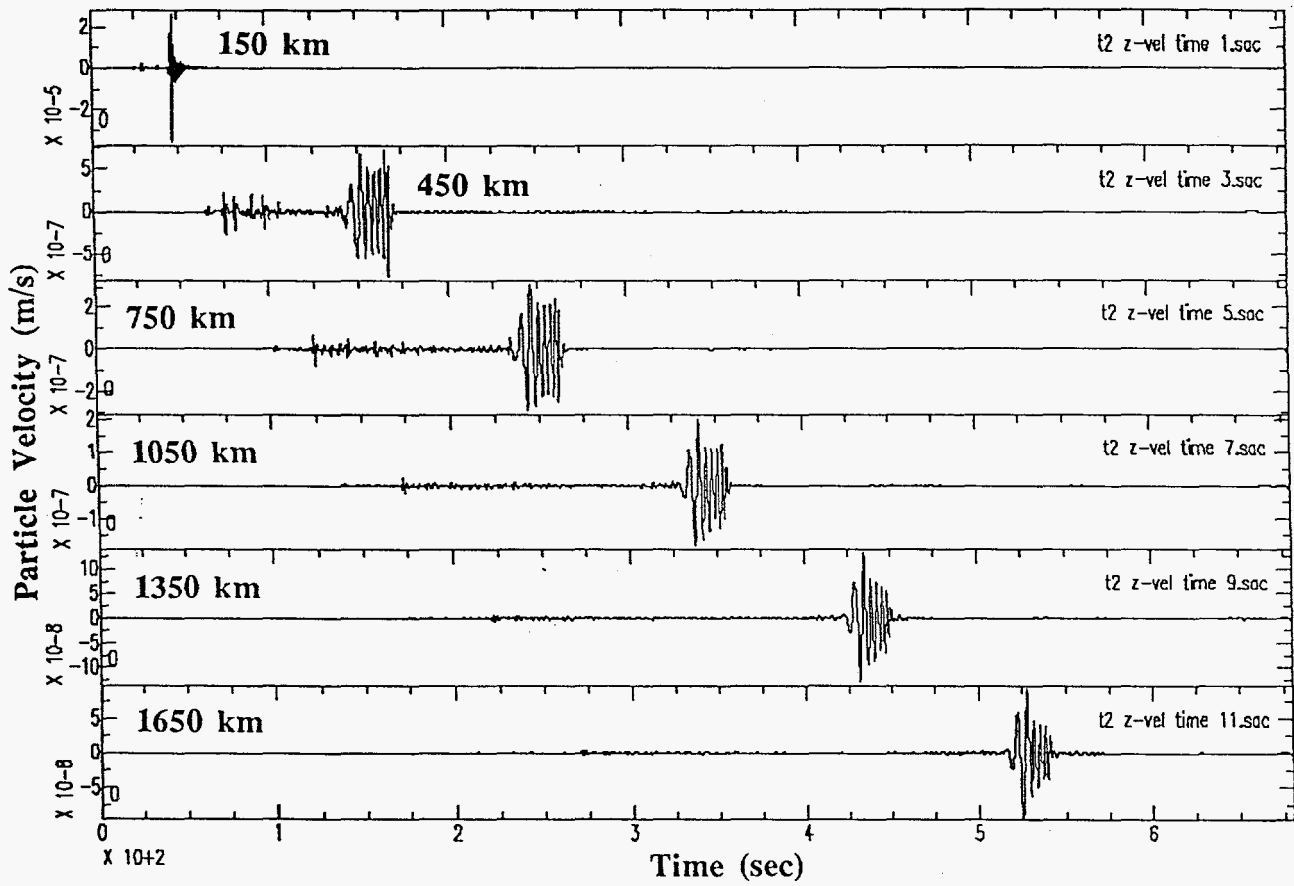
Fig. 26 Evolution of the seismic signal along the surface from 150 to 1650 km range for TLY21 calculation. Vertical component with scaling at each distance adjusted to peak amplitude.

Fig. 27 Evolution of the seismic signal at 20 km depth from 150 to 1650 km horizontal range for TLY21 calculation. Vertical component with scaling at each distance adjusted to peak amplitude.

Fig. 28 Evolution of the seismic signal along the surface from 150 to 1650 km range for NIL21 calculation. Vertical component with scaling at each distance adjusted to peak amplitude.

Fig. 29 Evolution of the seismic signal at 20 km depth from 150 to 1650 km horizontal range for NIL21 calculation. Vertical component with scaling at each distance adjusted to peak amplitude. The lines represent the same velocities shown in Figure 28.
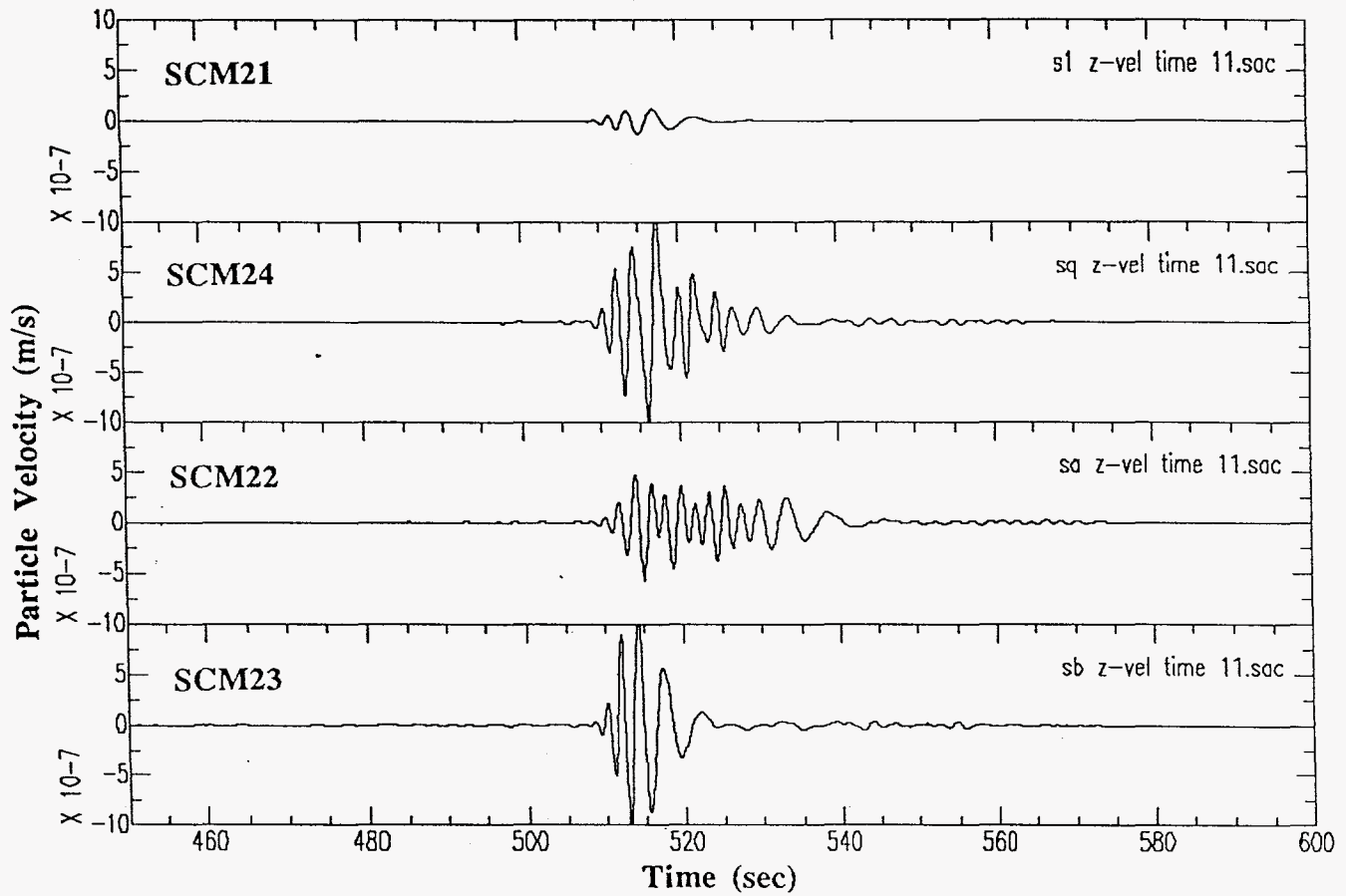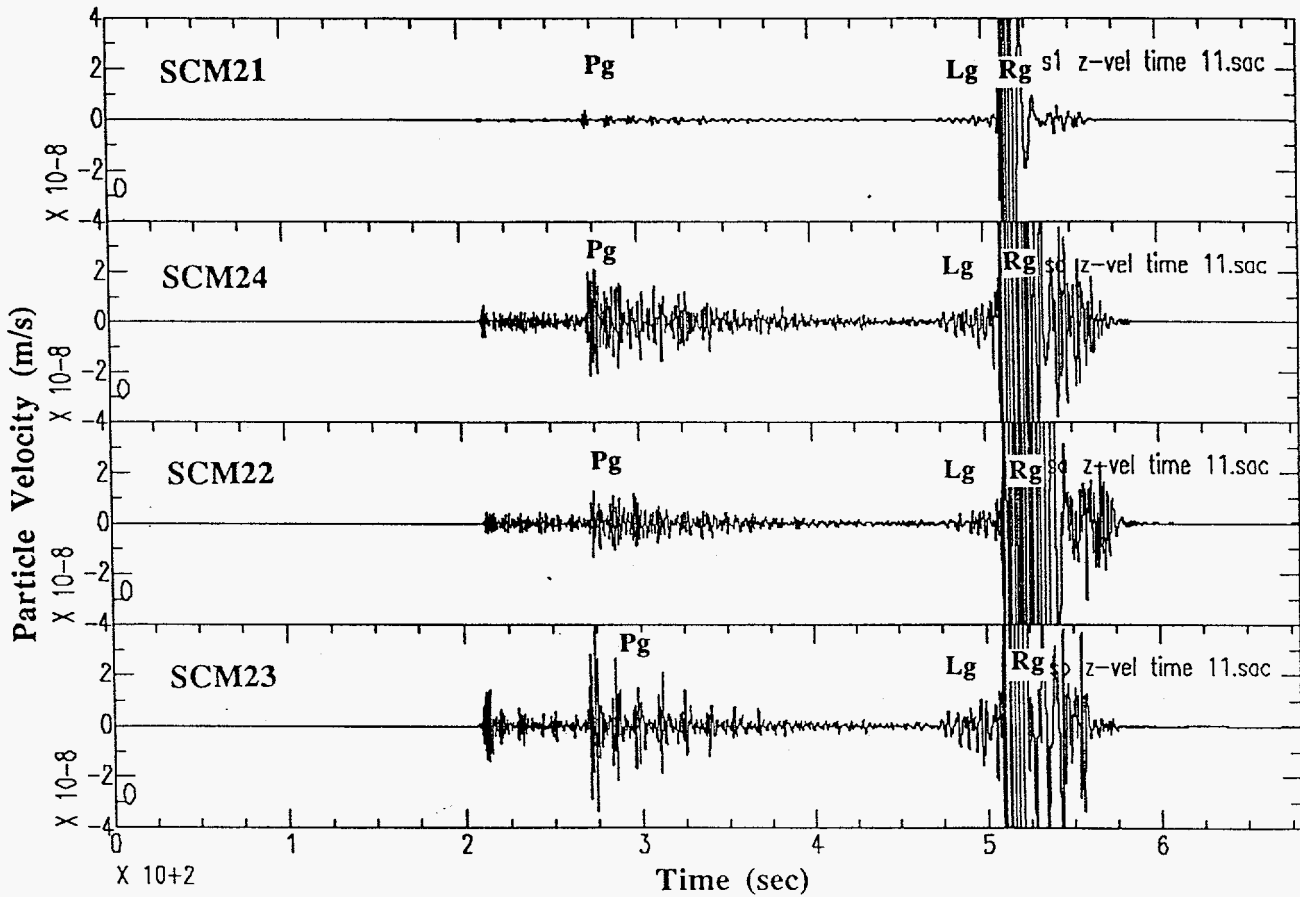
Fig. 30 Comparison of Rg phases (450 to 600 sec) at 1650 km for SCM21, SCM24, SCM22, and SCM23 calculations (same regional path, different source environments). Vertical component at the surface. Fixed amplitude scaling to the velocity range -1 x 10⁻⁶ to 1 x 10⁻⁶ m/s.

Fig. 31 Comparison of Pg and Lg phases at 1650 km for SCM21, SCM24, SCM22, and SCM23 calculations (same regional path, different source environments). Vertical component at the surface. Fixed amplitude scaling to the velocity range -4×10^{-8} to 4×10^{-8} m/s.
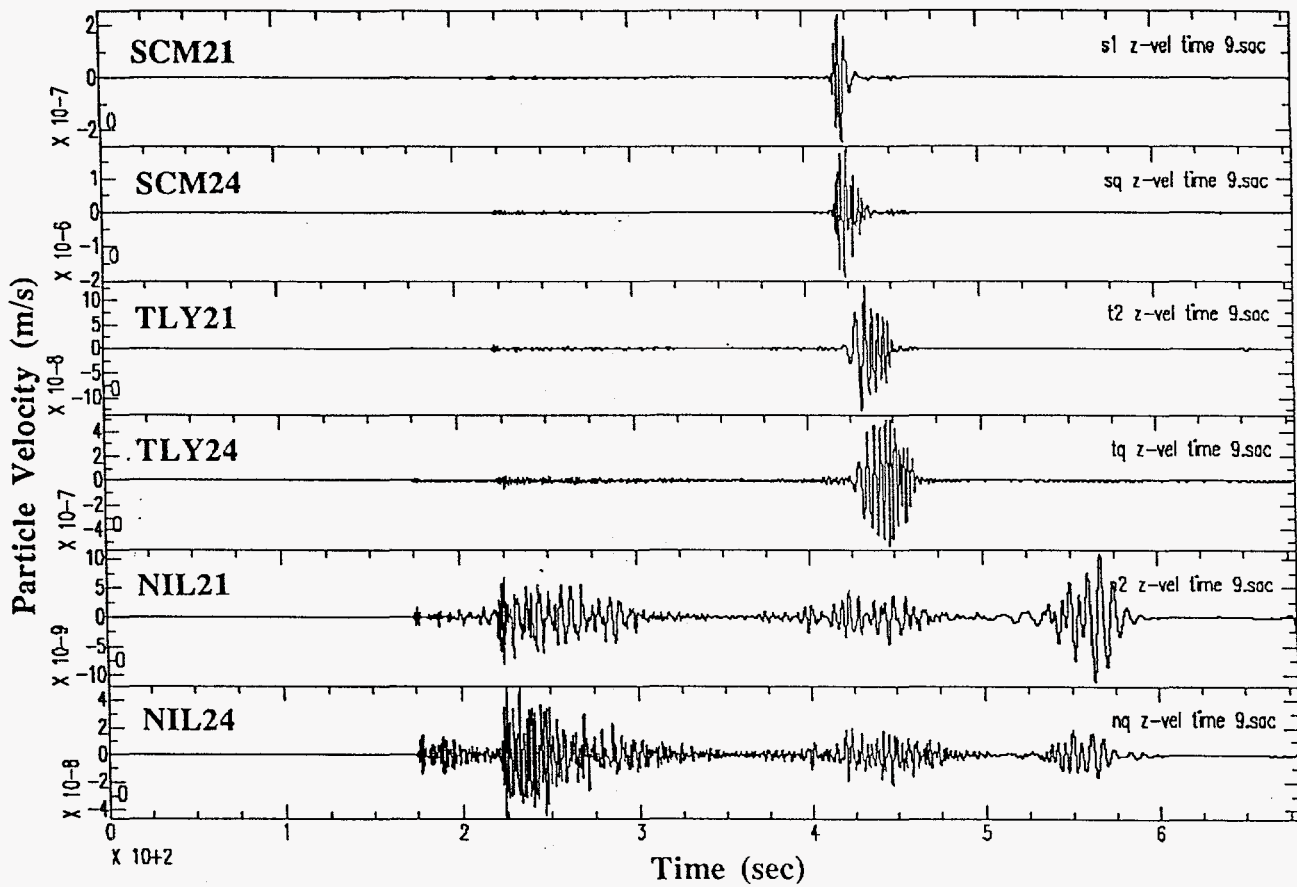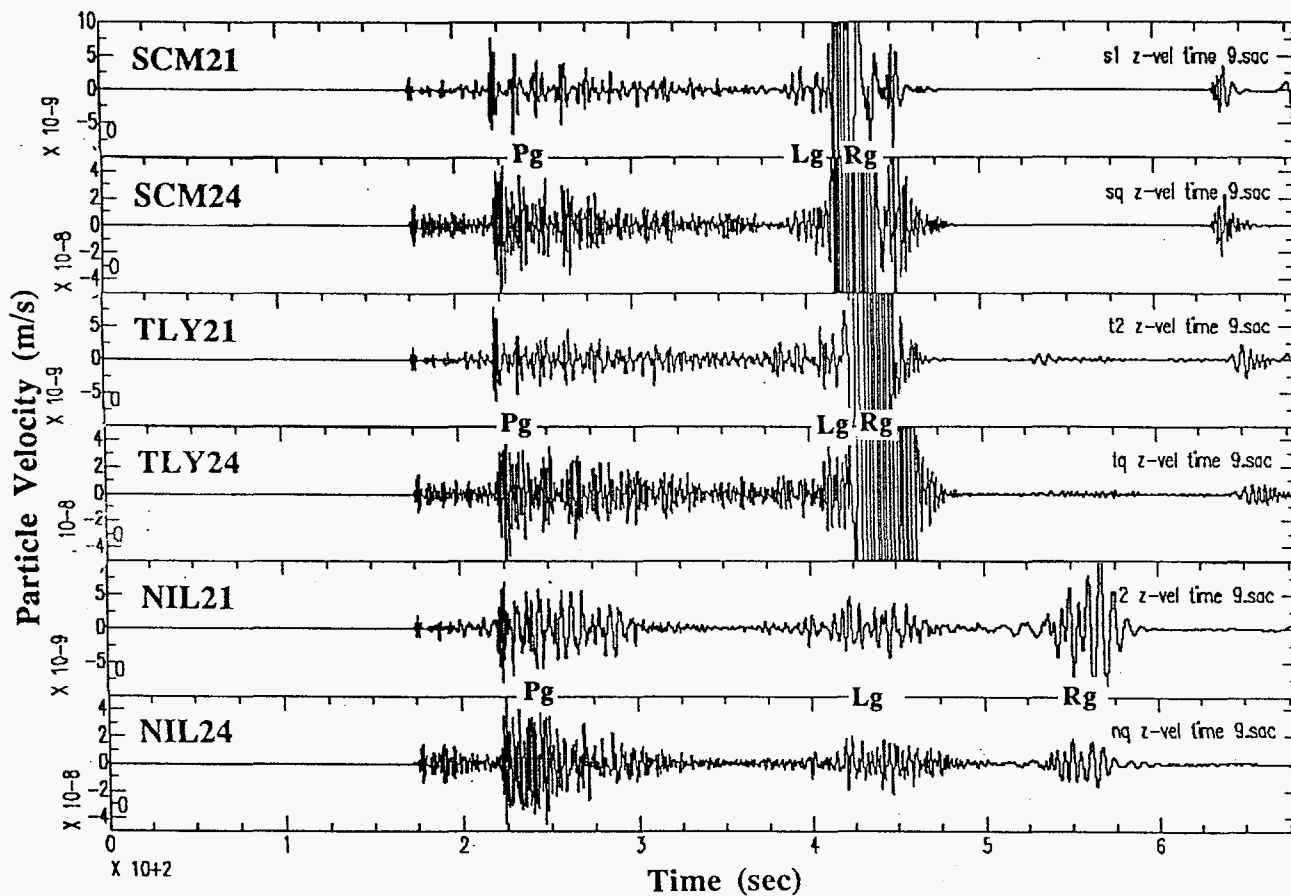
Fig. 32 Comparison of synthetic seismograms at 1350 km for SCM21, SCM24, TLY21, TLY24, NIL21, and NIL24 calculations (shows combined source and path effects). Vertical component at the surface. Plot scaling adjusted to peak amplitudes.
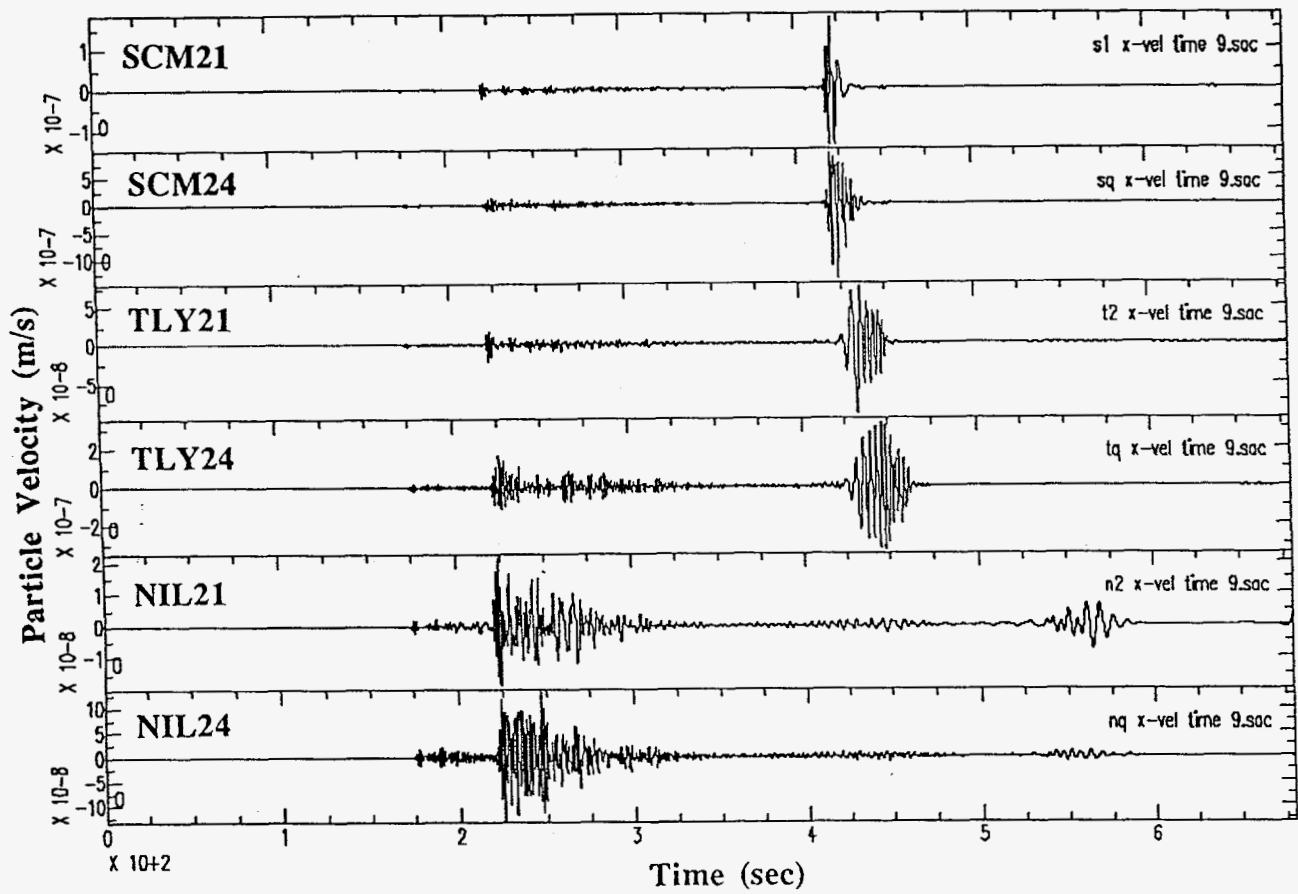
Fig. 33 Comparison of synthetic seismograms at 1350 km for SCM21, SCM24, TLY21, TLY24, NIL21, and NIL24 calculations (shows combined source and path effects). Vertical component at the surface. Fixed amplitude scaling to the velocity range -5 x 10⁻⁸ to 5 x 10⁻⁸ m/s for 24 series, -1 x 10⁻⁸ to 1 x 10⁻⁸ m/s for 21 series.

Fig. 34 Comparison of synthetic seismograms at 1350 km for SCM21, SCM24, TLY21, TLY24, NIL21, and NIL24 calculations (shows combined source and path effects). Horizontal component at the surface. Plot scaling adjusted to peak amplitudes.
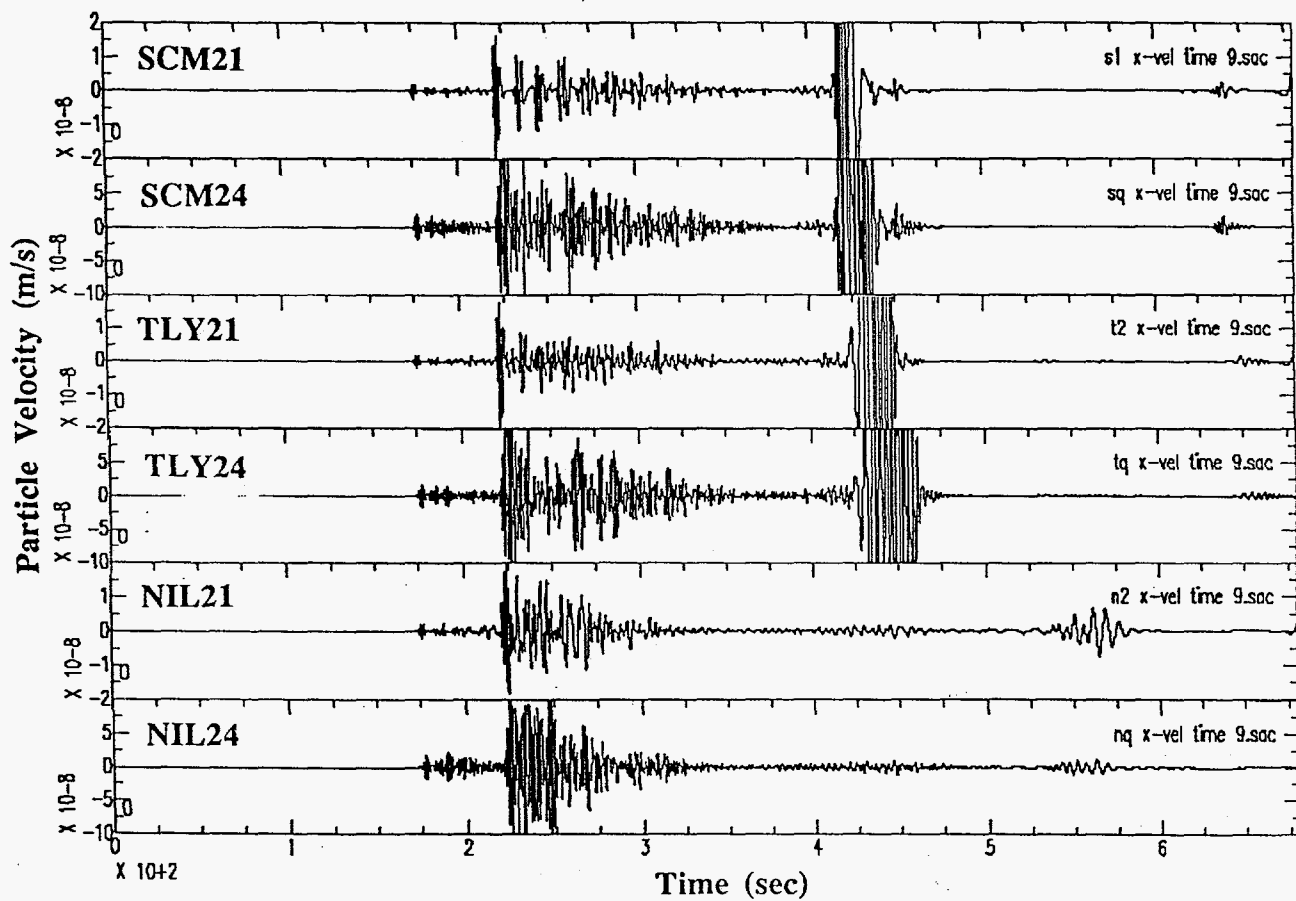
Fig. 35 Comparison of synthetic seismograms at 1350 km for SCM21, SCM24, TLY21, TLY24, NIL21, and NIL24 calculations (shows combined source and path effects). Horizontal component at the surface. Fixed amplitude scaling to the velocity range -1 x 10^{-7} to 1 x 10^{-7} m/s for 24 series, -2 x 10^{-8} to 2 x 10^{-8} m/s for 21 series.